COSEISMIC DEFORMATION OF THE 2002 DENALI FAULT EARTHQUAKE:

CONTRIBUTIONS FROM

SYNTHETIC APERTURE RADAR SPECKLE TRACKING

By

Julie Elliott

RECOMMENDED:

Advisory Committee Chair

Chair, Department of Geology and Geophysics

APPROVED:

Dean, College of Natural Science and Mathematics

Dean of the Graduate School

July 1, 2005

Date

COSEISMIC DEFORMATION FROM THE 2002 DENALI FAULT EARTHQUAKE : CONTRIBUTIONS FROM SYNTHETIC APERTURE RADAR SPECKLE TRACKING

A

THESIS

Presented to the Faculty

of the University of Alaska Fairbanks

in Partial Fulfillment of the Requirements

for the Degree of

MASTER OF SCIENCE

By

Julie Elliott, B.A.

Fairbanks, Alaska

August 2005

Abstract

The technique of speckle tracking can provide coseismic surface offsets for an earthquake in regions where other geodetic data are not available. These offsets can be used to map the surface deformation and create slip distribution models. This thesis uses speckle tracking to study the 2002 M_w7.9 Denali Fault earthquake, with emphasis on the central section of the rupture.

The Denali Fault earthquake began with a thrust event on the Susitna Glacier fault before rupturing unilaterally west to east on the Denali and Totschunda faults with overwhelmingly right-lateral strike-slip motion. A slip distribution estimated from a combination of speckle tracking data from the central section of the rupture, GPS data, and geologic data displays highly variable slip, with four major patches of high slip along the Denali fault. Compared to the primarily GPS-derived model of *Hreinsdóttir* [2005], the combined model is better constrained along the central rupture and predicts slip values much closer to the geologic offset measurements. A significant releasing bend in the fault just west of the pipeline can be correlated to a patch of high slip and the second-largest pulse of moment release along the rupture, suggesting that fault geometry plays an important role in earthquake mechanics.

Table of Contents

List of Figures

List of Tables

Acknowledgements

A number of people contributed to my research and this thesis. First and foremost, I would like to thank my advisor, Jeff Freymueller. He has taken time out of his hectic schedule to explain computer programming, look at preliminary results, and read over several drafts of this thesis. In addition, he has given me opportunities to get away from the computer and do some extraordinary field work. I've learned a lot over the past three years and am grateful for all of his help. My other committee members, Doug Christensen and Wes Wallace, taught me about earthquakes, kept my structural geology honest, and provided thoughtful reviews of my thesis even though for Wes that meant sending back comments from Rarotonga. Thank you! I'd also like to thank Bernhard Rabus of MacDonald Dettwiler and Associates for providing me with data, performing the initial processing, and answering questions along the way.

My undergraduate advisor, Fred Moore of Whitman College, and Tracy Vallier deserve many thanks for indulging my fascination with the Cascadia Subduction Zone and encouraging me to pursue geophysics. Without their support I would not be where I am today.

I'd like to thank the Alaska Volcano Observatory and John Eichelberger for allowing me to participate in two wonderful field trips to Katmai and Kamchatka. I'll never forget the experiences I had there.

I thank my friends and family for their support, particularly my brother, Doug, who has put up with many conversations centered around rocks, faults, and volcanoes both over the phone and on various hiking trips.

Finally, I'd like to thank the faculty, staff, and students of the Geophysical Institute for their support. I especially thank Sigrún Hreinsdóttir and Chris Larsen for all of their assistance and encouragement.

1 Introduction

In the early afternoon of November 3, 2002, an M_w7.9 earthquake struck the interior of Alaska. This earthquake, dubbed the Denali Fault earthquake, began with a thrust event on the previously unrecognized Susitna Glacier fault and ruptured almost 50 kilometers before jumping onto the right-lateral strike-slip Denali fault. The rupture then propagated eastward for about 240 kilometers before making another jump onto the right-lateral strike-slip Totschunda fault on which it continued for nearly 70 kilometers (Figure 1.1). In total, over 350 kilometers of ground ruptured in about 100 seconds. Surface offsets along the Denali fault increased in magnitude from west to east, reaching a maximum of 8.8 meters about 40 kilometers west of the junction between the Denali and Totschunda faults. Maximum surface offsets measured along the Susitna Glacier and Totschunda faults were smaller, about 5.4 meters and 3.1 meters, respectively [*Crone et al.*, 2004; *Haeussler et al.*, 2004].

The earthquake split through glaciers, caused massive landslides in the Alaska Range, resulted in seiches in lakes as far away as Louisiana, and triggered seismic activity in volcanic areas including Mt. Rainier in Washington state, Yellowstone caldera in Wyoming, and Long Valley caldera in California [*Eberhart-Phillips et al.*, 2003]. Fortunately, the sparse population in the rugged area around the fault meant that little property damage and no deaths occurred because of the earthquake.

The Denali Fault earthquake was a remarkable event in terms of both location and magnitude. Before November 3, only one earthquake with an $M \geq 5$ (the M_w6.7 October 23, 2002 Nenana Mountain earthquake) had occurred on the Denali fault since 1912. The earthquake was the largest in the (albeit brief) recorded history of interior Alaska, the largest strike-slip event in North America in nearly 150 years, and one of the largest in the world since the advent of modern technologies such as the Global Positioning System (GPS) and interferometric synthetic aperture radar (InSAR).

These attributes make the Denali Fault earthquake a tremendous opportunity to study the fault mechanics of a large strike-slip event. Key to any study of earthquake

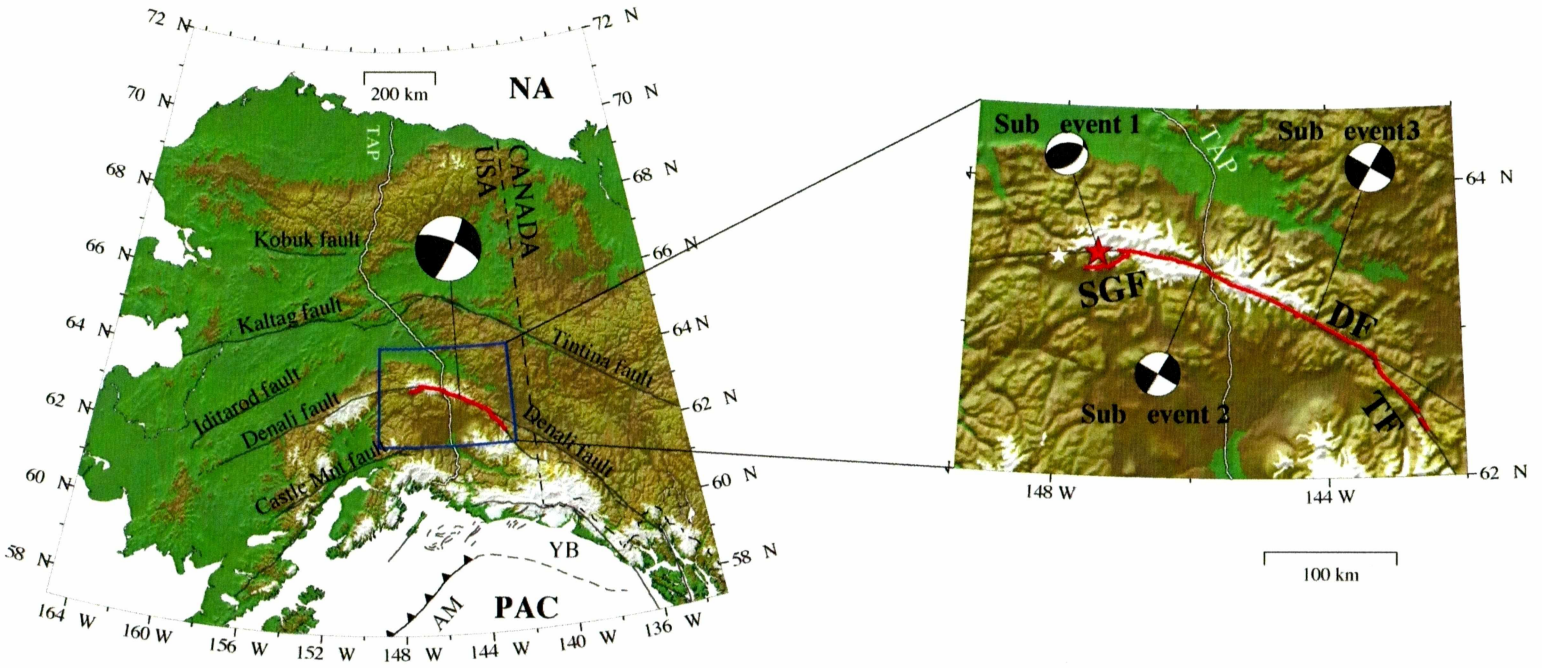

Figure 1.1. Tectonic setting of the Denali Fault earthquake. In the main map (left), major tectonic elements include the North American plate (NA), the Pacific plate (PAC), the Aleutian Megathrust (AM), the Yakutat Block (YB), and the strike-slip faults shown in black. The red line denotes the Denali Fault earthquake rupture [*Haeussler et al.*, 2004] and the focal mechanism is the Harvard CMT solution. In the inset (right), the red rupture line includes parts of three faults: the Susitna Glacier fault (SGF), the Denali fault (DF), and the Totschunda fault (TF). The white star marks the epicenter of the of M_w6.7 Nenana Mountain earthquake while the red star indicates the epicenter of the Denali Fault earthquake. Focal mechanisms shown are for the first motion solution (Sub-event 1) and the two largest sub-events found from waveform inversion (Sub-event 2 and Sub-event 3) [*Eberhart-Phillips et al.*, 2003]. The Trans-Alaska Pipeline (TAP) is shown for reference and the faults are taken from *Plafker et al.* [1994]. Topography is from U.S. Geological Survey TOPO30 data obtained from the National Geophysical Data Center.

mechanics is the development of a detailed and well-constrained slip model that shows how slip varies along the strike of the rupture and with depth, the location of asperities, and how structures such as bends in the fault impact slip. An essential ingredient to such a model is a set of coseismic surface displacement measurements.

Geologic surface offsets, GPS data, and InSAR data can all provide the necessary displacement measurements. In the case of the Denali Fault earthquake, all three types of data are available to varying degrees. *Haeussler et al.* [2004] discussed geologic surface offset observations for the Denali and Totschunda sections of the rupture while *Crone et al.* [2004] reported scarp heights along the Susitna Glacier thrust fault. Expanding the results of *Hreinsdóttir et al.* [2003], *Hreinsdóttir* [2005] and *Hreinsdóttir et al.* (submitted to the Journal of Geophysical Research) presented coseismic displacements estimated at 232 GPS sites throughout Alaska and Canada as well as a slip model derived from an inversion of the GPS data and selected geologic surface offset measurements. *Wright et al.* [2004] mapped surface deformation surrounding the western half of the rupture with five SAR interferograms and used the InSAR data in conjunction with 40 coseismic GPS measurements to construct slip models for the earthquake.

However, all of these datasets are limited in their spatial extent and do not yield a complete, encompassing set of surface displacement measurements for the entire rupture (Figure 1.2). Although GPS measurements exist from one end of Alaska to another, they are confined mainly to the road system, leaving large areas with few or no sites. The geologic surface offset measurements are limited to the rupture area and can only be made where offset features can be identified. In addition, certain subsets of those measurements have proven to be unreliable estimates of surface slip. *Haeussler et al.* [2004] found that the fabric of glacial ice influenced the location of the surface rupture. By comparing glacial offset measurements to GPS displacements on the Black Rapids Glacier, *Hreinsdóttir* [2005] determined that this influence often resulted in underestimated surface offset values. The young, saturated fluvial deposits in the area of the Trans-Alaska Pipeline and the thick Quaternary sediments around the region of the Tok Cutoff Highway caused broad zones of distributed deformation that resulted in offset

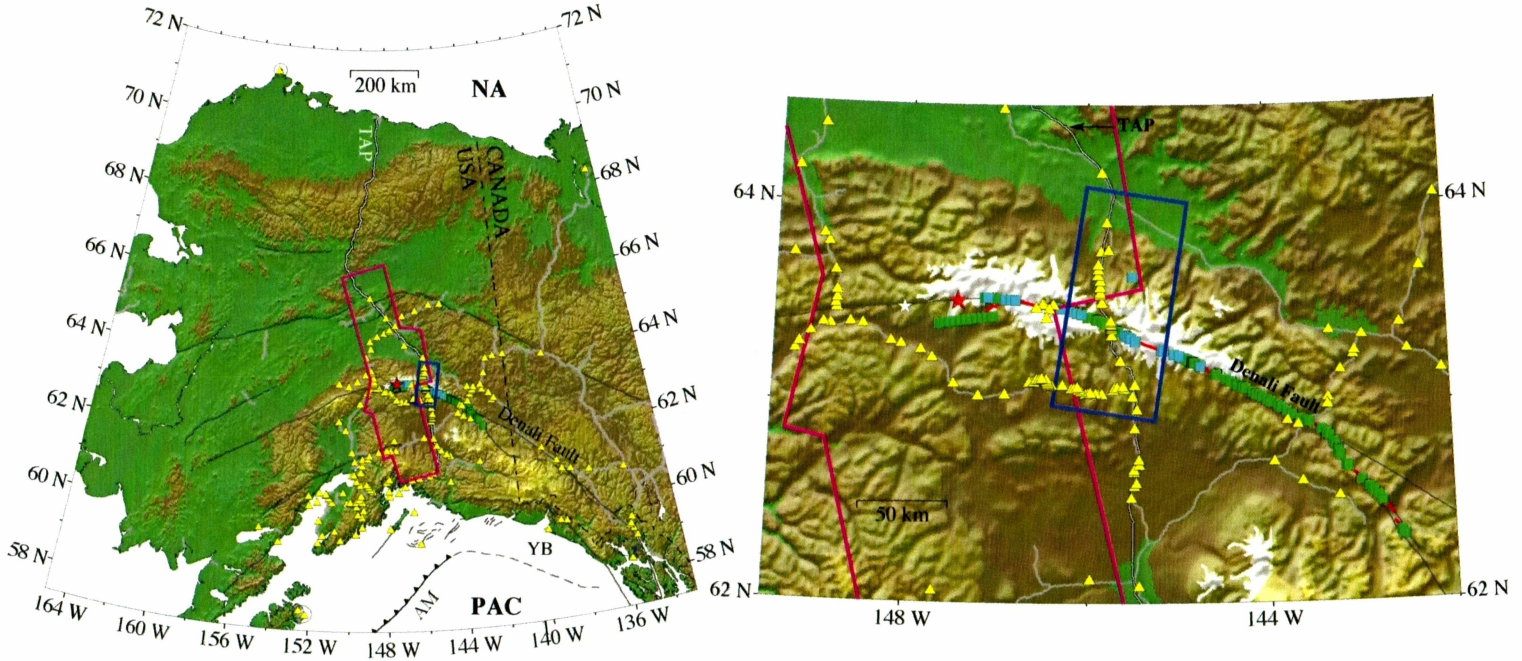

Figure 1.2. Coseismic data distribution for the Denali Fault earthquake. Major tectonic plates and boundaries are the North American plate (NA), Pacific plate (PA), the Aleutian Megathrust (AM), and the Yakutat Block (YB). Purple lines mark the extent of the InSAR data of *Wright et al.* [2004] while the blue box shows the boundaries of the speckle tracking data. Yellow triangles denote GPS sites, turquoise squares identify glacier offset measurements, and green boxes shown other geologic surface measurements. The white star marks the epicenter of the M_w6.7 Nenana Mountain earthquake and the red star is the epicenter of the Denali Fault earthquake. The Trans-Alaska Pipeline is shown for reference. Faults are taken from *Plafker et al.* [1994]. The map on the right shows an enlarged view of the faults ruptured by the earthquake and the area considered in this study.

values that did not record the full slip [*Haeussler et al.*, 2004]. The five InSAR scenes presented by *Wright et al.* [2004] only cover the western half of the rupture, ending around the Trans-Alaska Pipeline. Within this coverage area, incoherence caused by high relief, glaciers, and the shear magnitude of the displacements destroyed the usefulness of the data immediately adjacent to the fault [*Wright et al.*, 2005]. These gaps in the surface displacement data lead to slip distribution models with areas of low resolution.

The technique of SAR speckle tracking can provide surface displacement measurements to fill in the gaps. Speckle tracking uses the offsets between two SAR amplitude images acquired before and after the earthquake to determine the ground displacements. Since speckle tracking utilizes amplitude rather than phase, phase-related problems, such as image decorrelation in areas where the ground cover changed (e.g. from snowfall) or with large deformation gradients, do not occur. Consequently, speckle tracking has the potential to deliver more usable data than InSAR in the regions closest to the fault. Several authors have used speckle tracking to study strike-slip earthquakes with $M > 7$. *Peltzer et al.* [1999] mapped the surface rupture of the 1997 M_w7.6 Manyi, Tibet earthquake with SAR amplitude offsets. *Michel et al.* [1999a,b] described the method for determining surface displacements from amplitude image offsets and applied the technique to the 1992 Landers earthquake, an M_w 7.3 event. Although the SAR amplitude offset measurements had larger uncertainties than the GPS data, the authors found that an offset-derived model fit the GPS data nearly as well as a GPS-derived model because of the high spatial density of the offset data, particularly near the fault. *Jónsson et al.* [2002] used SAR amplitude offsets to prove that the geologic offset measurements had been underestimated in the field, derive an offset-based fault model, and constrain fault geometry and near-fault displacements in a combined InSAR/GPS/SAR offset slip model for the 1999 M_w7.1 Hector Mine earthquake.

In this thesis, I use the technique of speckle tracking to study earthquake-related deformation around the central section of the 2002 Denali Fault earthquake rupture. First, I map the surface deformation using SAR speckle tracking offsets. With these deformation measurements, I construct cross- and along-strike data profiles to examine

the magnitude of the slip and how slip varies along the rupture, with emphasis on the junction of the Denali fault with the Trans-Alaska Pipeline and Richardson Highway. From this, I determine how robust the speckle tracking offset data are relative to the GPS measurements and how well the offsets can serve as substitutes for or complements to the GPS data in areas with few or no GPS sites. To compare the speckle tracking results to the geologic surface measurements, I convert the speckle tracking offset data into a full lateral slip estimate. Finally, I combine the speckle tracking offset data with the GPS data and geologic surface measurements to estimate a slip distribution for the earthquake, contrast this model with several other models derived from GPS, InSAR, geologic, and seismic data, and explore what new information the speckle tracking results provide about the earthquake and rupture mechanics.

2 Tectonic Background

The Denali Fault system is the largest in a series of arcuate, dextral transcurrent faults related to the shift from transform motion along the Fairweather-Queen Charlotte Fault system to convergent motion along the Aleutian Megathrust in southern Alaska (Figure 1.1). In the complex transition zone between the two tectonic regimes, the Yakutut Block, a composite oceanic and continental terrane, is currently colliding with and deforming the North American plate [*Plafker and Berg,* 1994; *Fletcher and Freymueller*, 2003]. Stretching over 2,000 kilometers from the Bering Sea to southeast Alaska, the Denali fault system borders the highest topography in North America, slices through rock ranging in age from Precambrian to Quaternary, and has played a major role in displacing tectonostratigraphic terranes after their accretion to North America.

Evidence for pre-Tertiary motion along the Denali system is tenuous and *Lanphere* [1978] suggested that it is primarily a post-Mesozoic structure. Correlations between terranes in Alaska and the Yukon Territory of Canada and offset plutons near Mt. McKinley imply up to 400 kilometers of dextral displacement during the Tertiary, with a probable reduction of the slip rate after 38 Ma [*Forbes et al.*, 1973; *Reed and Lanphere*, 1974; *Turner et al.*, 1974; *Nokleberg et al.*, 1985]. Well-documented evidence

for motion during the Holocene exists for the central section of the Denali system (comprised of the McKinley and western Shakwak segments of the fault) and for the Totschunda fault. The McKinley segment, which includes part of the 2002 earthquake rupture, has been one of the most active sections of the Denali system during the last 10,000 years. Based on scarps and offset stream channels, *Stout et al.* [1973] postulated up to 50-60 meters of dextral motion and 6-10 meters of vertical displacement (north side up) near the Delta River and Richardson Highway corridor during the Holocene. To the west, around the Nenana River and Parks Highway, *Hickman et al.* [1977] documented 110-230 meters of dextral displacement and 3-5 meters of vertical motion (south side up), but their estimates for the timing of this motion are fairly uncertain. Recent paleoseismic investigations on the Denali fault east of 143°W (east of the 2002 rupture) found evidence of Holocene slip (D. Schwartz, personal communication), although fault slip rates have not been published. A substantial fraction of the fault motion along the eastern portion of the Denali fault system seems to have transferred onto the Totschunda fault, where *Richter and Matson* [1971] found offset glacial features indicating 110-350 meters of dextral displacement since the late Pleistocene.

Prior to the 2002 earthquake sequence, the level of recorded seismicity along the Denali system was very low, particularly along the central Denali fault in the region of the 2002 rupture. From 1912 to 2002, only one possible strike-slip event of $M > 5.5$ occurred on the fault. This earthquake, an M_s 7.2 in 1912, had parameters consistent with shallow, right-lateral slip, but the data did not exclude other focal mechanisms and the location error ellipse extended from about 144.5°W to 149.5°W [*Doser*, 2004]. Tree ring counts from split and tilted spruce trees close to the fault support right-lateral strike-slip motion on or near the Denali fault in 1912 [*Plafker et al.*, 2004].

Estimates of the pre-earthquake slip rate have varied. Information about prior large Denali fault earthquakes obtained from test pits along the Delta River initially led *Plafker et al.* [2004] to suggest an average long term slip rate of about 15 mm/yr, but the authors later revised this estimate down to about 10 mm/yr [*Plafker*, oral comm., 2004]. Data from triangulation networks straddling sections of the McKinley segment showed

no evidence of significant right-lateral slip during the 1970's or 1980's [*Page*, 1972; *Savage and Lisowski*, 1991]. Based on GPS measurements made between 1995 and 2002, *Fletcher* [2002] postulated a present-day slip rate of 6-9 mm/yr on the Denali fault. A recent study of cosmogenic ^{10}Be in boulders and sediment from displaced moraines along the Denali and Totschunda faults found an average slip rate of 9 to 13 mm/yr on the Denali fault and 6 mm/yr on the Totschunda fault since the late Pleistocene [*Matmon et al.*, 2004]. The authors attribute the difference in rate between the Denali and Totschunda faults to a partitioning of slip between the two faults east of their junction, which suggests a slip rate of 3 to 7 mm/yr on the Denali fault east of the 2002 rupture.

3 Overview of SAR and Speckle Tracking

At the heart of space-borne SAR is the radar platform itself: a satellite that illuminates a target with microwave-frequency electromagnetic waves and then collects the signal returned from the target. The amplitude of the backscattered signal and the signal's round trip travel times reveal properties of the target and its surroundings and yield the distance between the satellite and target. A conventional radar system orbiting at the typical height of 1000 kilometers above the earth can provide a ground resolution of about 5-10 kilometers, a resolution that is much too low to be useful in geophysical applications. Obtaining a ground resolution of a few tens of meters would require the conventional radar to have an antenna (or aperture) length on the order of 1 to 2 kilometers, far too large to be practical. SAR solves this problem with a mathematical trick during the signal processing. The SAR satellite images a target multiple times as it travels from point A to point B (Figure 3.1). Summing these images over the distance (B-A) produces the same resolution as a radar antenna stretching from A to B.

The geometry of the radar is integral to both the processing and the geophysical interpretation of the images (Figure 3.2). The satellite travels along its orbital trajectory (the along-track or azimuth direction) while it illuminates targets along the cross-track or range direction. Space-based SAR employs side-looking radar; RADARSAT, the satellite used in this study, looks to the right. The incidence angle (measured from local vertical)

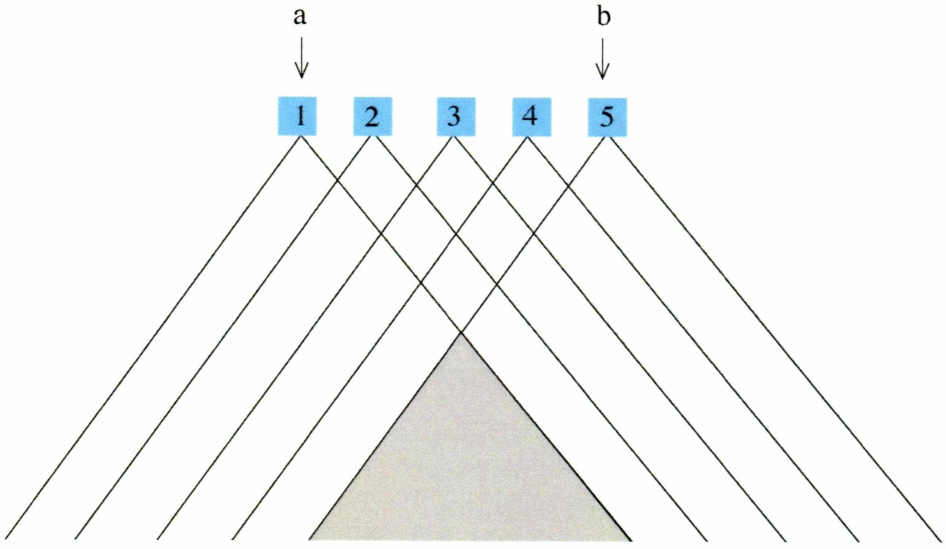

Figure 3.1. How SAR works. As it moves from point a to point b, the satellite emits five radar pulses. Each pulse illuminates the shaded area. Summing the images over this area produces the same ground resolution as an antenna stretching from a to b.

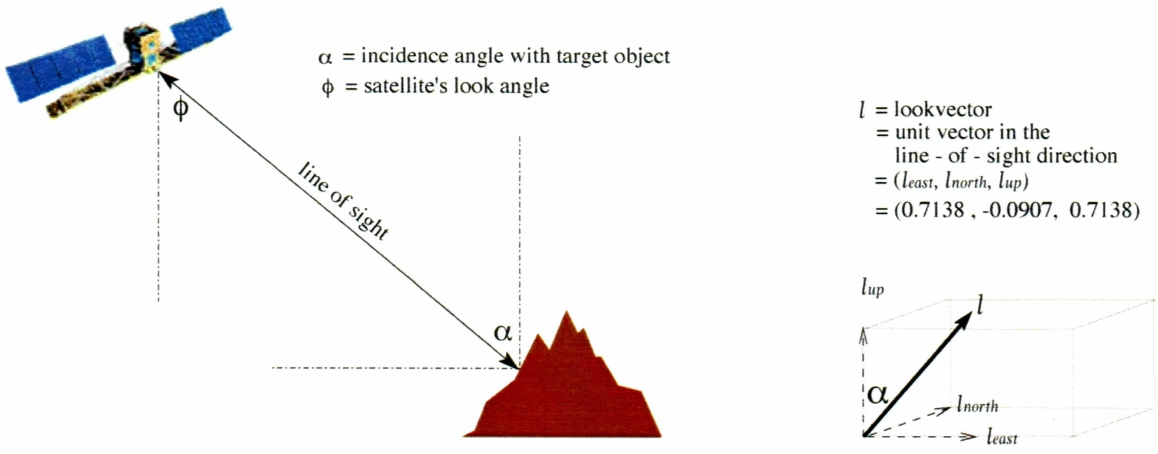

Figure 3.2. Schematic of SAR geometry. The incidence angle is slightly larger than the look angle due to the curvature of the earth. Both the incidence angle and the look angle increase with the distance from the satellite in the range direction across the image. The east, north, and up components of the mean look vector for the image used in this study are [0.7138, -0.0907, 0.7138].

between the radar beam and the target defines the look vector, which is a unit vector pointing in the line-of-sight direction. Line-of-sight (LOS) is an extremely important concept in SAR studies; all changes in the distance between the satellite and target are measured along this direction instead of in the more familiar east, north, up coordinate system.

A SAR image contains information about both the phase of the returned radar signal and the amplitude of the signal, a measure of how completely a ground target sends the incident signal back to the radar. While InSAR uses phase differences between two images to create contour maps of surface deformation, speckle tracking exploits the pattern of returned amplitudes to track how targets have shifted from one image to another. If the incident signal encounters a target such as a calm, smooth lake, the signal will reflect perfectly off the surface, away from the radar. No signal returns to the radar, creating a dark area in the radar image. If the incident beam intersects a craggy rock outcrop, it will scatter in many different directions, including back towards the satellite. This returned signal creates a bright area in the radar image. The greater the amount of signal returned, the brighter the area in the image.

The key to speckle tracking is the precise alignment of two SAR images. This is achieved through the technique of cross-correlation. First, both images are divided into 'pixel chips', which are relatively small groups of pixels (Figure 3.3). Since the cross-correlation procedure involves the use of Fourier transforms, the dimensions of the pixel chips must be powers of two. Next, the reference chip is moved pixel-by-pixel throughout the search chip. For each reference pixel-search pixel combination, the correlation index (CI), a measure of how well the features of the reference chip match those of the search chip, is calculated. *Moick* [1980] defined the CI as

$$\mathrm{CI}_{(\mathrm{L,S})} = \frac{\sum_{l,s}(r_{(l,s)} - \mu_r)(s_{(l,s)} - \mu_s)}{\left[\sum_{l,s}(r_{(l,s)} - \mu_r)^2\right]^{1/2}\left[\sum_{l,s}(s_{(l,s)} - \mu_s)^2\right]^{1/2}}$$

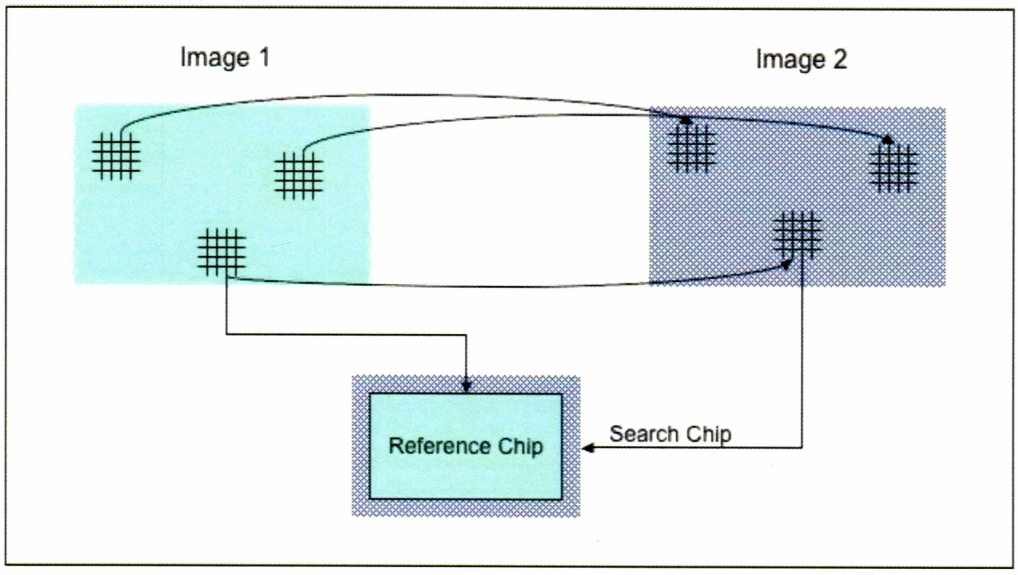

Figure 3.3. Diagram of pixel chips used in cross-correlation. Curved arrows show corresponding pixel chips in the two images.

where $CI_{(L,S)}$ is the correlation index between the reference and search chips at the search chip center pixel locations L,S; $r_{(l,s)}$ equals the DN (digital number, a measure of the brightness of the amplitude that ranges from 0 to 2) of the reference chip pixel at location *l*,*s*; μ_r is the average DN for the reference chip; $s_{(l,s)}$ equals the DN of the search chip pixel at location *l*,*s*; μ_s is the average DN for the search chip; and *l*,*s* are the dimensions of the reference chip. As the reference and search chips reach the correct alignment, the CI approaches a maximum ($CI \leq 1$). If the CI values are plotted against the position of the reference chip, this maximum CI value defines a first-order estimate of the x-y (range-azimuth) offset for the area of the pixel chips (Figure 3.4). Fitting a biquadratic function around the peak of the CI values will yield a local offset estimate accurate to within about a tenth of a pixel.

Theoretically, this process results in a successful correlation and local offset estimate for each pixel chip area defined. In reality, however, false correlations occur because of statistically featureless pixel chips that are difficult to match, or distortion of one or both images. To avoid having false correlations propagate into false offsets, a minimum acceptable CI peak must be defined and the cross-correction procedure must be performed in both the forward and reverse directions. If the maximum CI values fail to reach the threshold or the forward and reverse correlations produce different offset values, the correlation has to be rejected. The number of defined reference chips can far exceed the number of valid correlations, so the randomly scattered offset values are interpolated throughout the image to create a spatially dense offset map.

This dense map does come at a price: speckle tracking data has an inherently higher level of noise than InSAR data. Average uncertainty for speckle tracking data is about a tenth of a pixel, or 0.8 meters in range and 0.4 meters in azimuth [*Michel et al*, 1999a], while average uncertainty for InSAR data typically ranges from a few to a few tens of millimeters. Previous speckle tracking studies (e.g., *Michel et al.,*1999a; *Jónsson et al*., 2002) only used offsets in the azimuth direction for two reasons. First of all, the magnitude of the ground displacement in the range direction fell below the noise level of the data. This was primarily because the faults in these cases (parts of the San Andreas

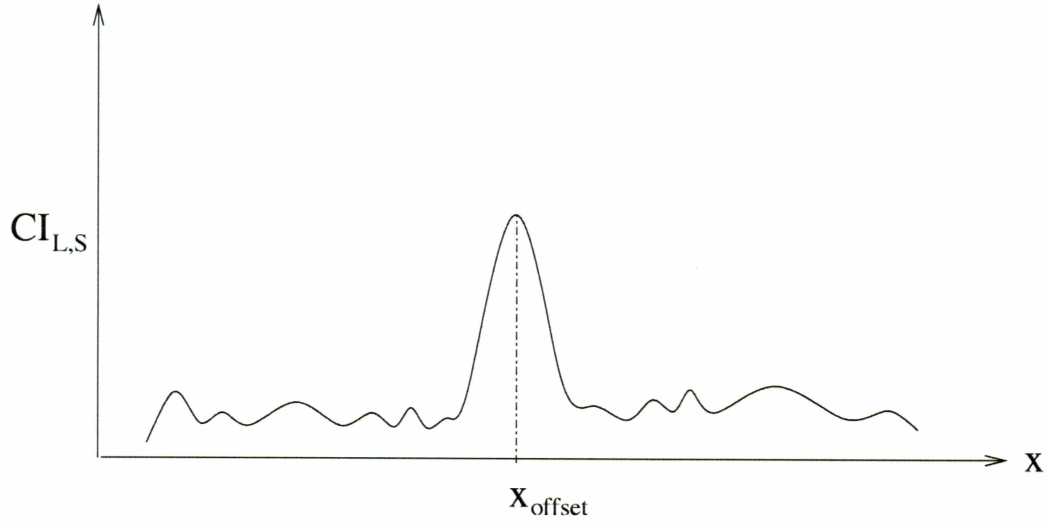

Figure 3.4. Schematic of an offset peak. In this case, x represents distance in the range direction. The x-value beneath the maximum CI value gives an estimate of the local range offset.

system) were mostly oriented sub-parallel to the azimuth direction and strike-slip motion creates displacements parallel to the fault. In constrast, the Denali fault is sub-parallel to the range direction. Secondly, azimuth offsets provide information perpendicular to the radar's look direction while range offsets lie parallel to the look direction, offering little additional information to the InSAR data. However, range offsets do add valuable data in areas with little or no InSAR coverage, such as the central and eastern portions of the Denali rupture. This, combined with the orientation of the fault and the fact that the magnitude of the displacements overwhelms the average uncertainties, makes the range offsets a useful tool for studying the 2002 Denali Fault earthquake.

4 Speckle Tracking Data

I used data acquired by the Canadian radar satellite RADARSAT-1 on 24 October 2002 and 4 January 2003 from descending (southward-trending) orbits. At the time of acquisition, the satellite was in fine mode, using a high bandwidth radar signal in order to improve resolution in the range direction. This choice of beam mode resulted in input imagery with a ground resolution of about 8 meters. Unfortunately, fine mode data only existed along the central section of the 2002 earthquake rupture, limiting my study area (Figure 1.2). However, this region serendipitously included a number of interesting features such as the intersection of the fault with the Trans-Alaska Pipeline, two major bends in the fault, and GPS networks along the northern Richardson Highway and the Denali Highway that can be used for ground truthing. The incidence angle varied from 43.1 degrees to 45.5 degrees across the image, with the magnitude of the angle decreasing away from the satellite. Correspondingly, the look vector changes with position in the cross-track direction and has an average value (east, north, up) of [0.7138 -0.0907 0.7138] (Figure 3.2).

5 Data Processing

5.1 Initial Processing

The raw range offset map was created by Bernhard Rabus of MacDonald Dettwiler and Associates (MDA) using MDA's FASTCOR algorithm to perform a fast cross-correlation on the two image scenes. In coherent areas where the ground surface did not greatly change, the matching process could successfully proceed with or without the presence of macroscopic features. Matching in incoherent regions that experienced substantial surface change required the presence of macroscopic features such as ridges, lake shorelines, or roads. The quality of matching in these areas was generally lower because the incoherent speckle acted as noise. Each correlation pixel chip had dimensions of 64 pixels by 64 pixels or 500 meters by 500 meters. Pixels within each chip are highly correlated with each other, so completely independent data observations are located more than 64 pixels or 500 meters apart from one another. The maximum accuracy of the offsets is about 1/32 of a pixel or ± 0.25 meters. This accuracy value reflects how successfully the cross-correlation process picked out the peaks of the CI curves. After cross-correlation, the data were decimated to produce an image containing 17,780,940 pixels, each with dimensions of 25 meters by 25 meters (Figure 5.1).

5.2 Preliminary Data Reduction

A total of nearly 18 million data points caused serious computational difficulties and made analysis impractical, so I used a 5-pixel by 5-pixel averaging window and then selected the center point of each averaged section to reduce the data to a 1,245-pixel by 571-pixel grid. Each pixel then represented an area of 125 square meters. Although this averaging and reduction only left about 4% of the original data points, no significant information was lost since the data were so highly correlated spatially. The averaging reduced random noise in the image, but any systematic errors in the data remained.

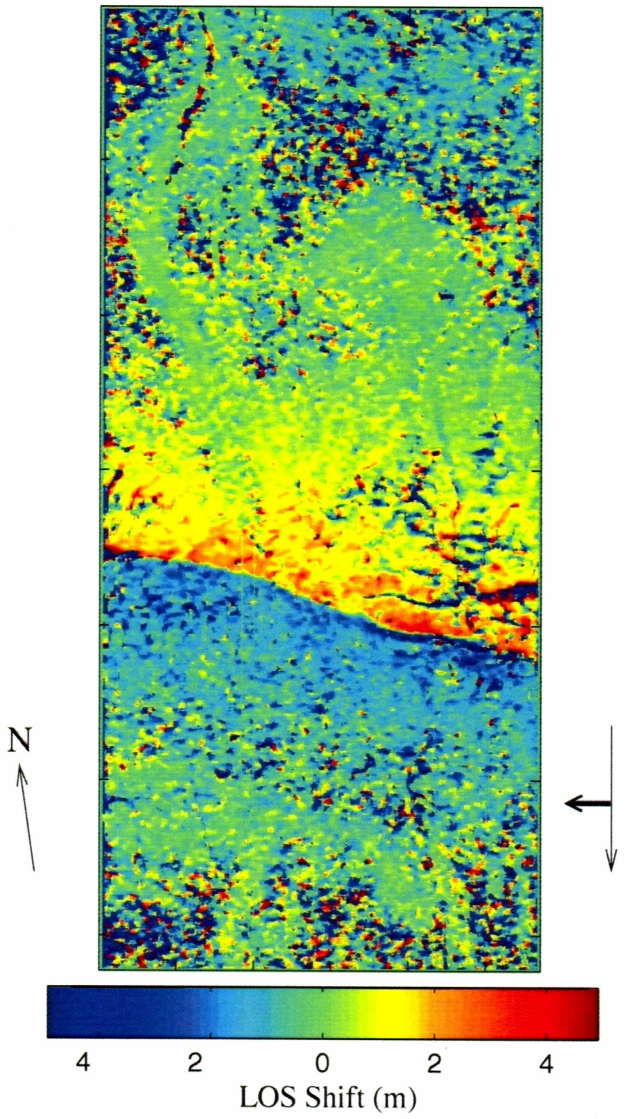

Figure 5.1. Raw offset map. The thin arrow shows the direction of the satellite's flight path while the thick arrow indicates the look direction.

5.3 Masking the Data

Despite the measures taken to avoid them, some false correlation matches did occur. These false offsets appeared in the offset map as pixels with values orders of magnitude different from the typical values between -5 and 5 meters. I determined that the false offsets biased other offsets located up to five pixels away, a probable consequence of interpolation between offsets during the cross-correlation procedure. To remove the false offsets and all pixels possibly affected by them, I located each outlier point (defined as |pixel value| > 5 meters) and masked out an 11-pixel by 11-pixel area centered on that point.

5.4 Filtering

An examination of how displacement values varied in the range direction revealed a nearly periodic signal in the data (Figure 5.2a). As the signal occurred throughout the image irrespective of the local magnitude of the earthquake displacements, it represented a systematic error. To investigate this signal, I constructed autocorrelation plots for a sampling of the range lines (rows of the image). These plots showed a regularly undulating signal whose amplitude and wavelength gradually tapered off away from the origin. The signal only appeared in range lines, not in azimuth lines. Since range offsets are sensitive to displacements parallel to the radar's look direction while azimuth offsets are not, the observed signal suggested a spurious frequency in the radar beam itself or one introduced during processing. *Michel et al.* [1999a] found a similar signal in a SAR offset map, but it was along the azimuth direction instead of the range. It is interesting to note that in both the present study and that of *Michel et al.* [1999a], the oscillations occurred in the direction parallel to the fault.

To isolate the wavelength or wavelengths causing the oscillations, I took the discrete Fourier transform of each range line, generated a power spectrum from the Fourier transform, and plotted the power spectrum against frequency. The power spectrum plots were then stacked. A peak between the wavelengths of 4,760 and 238

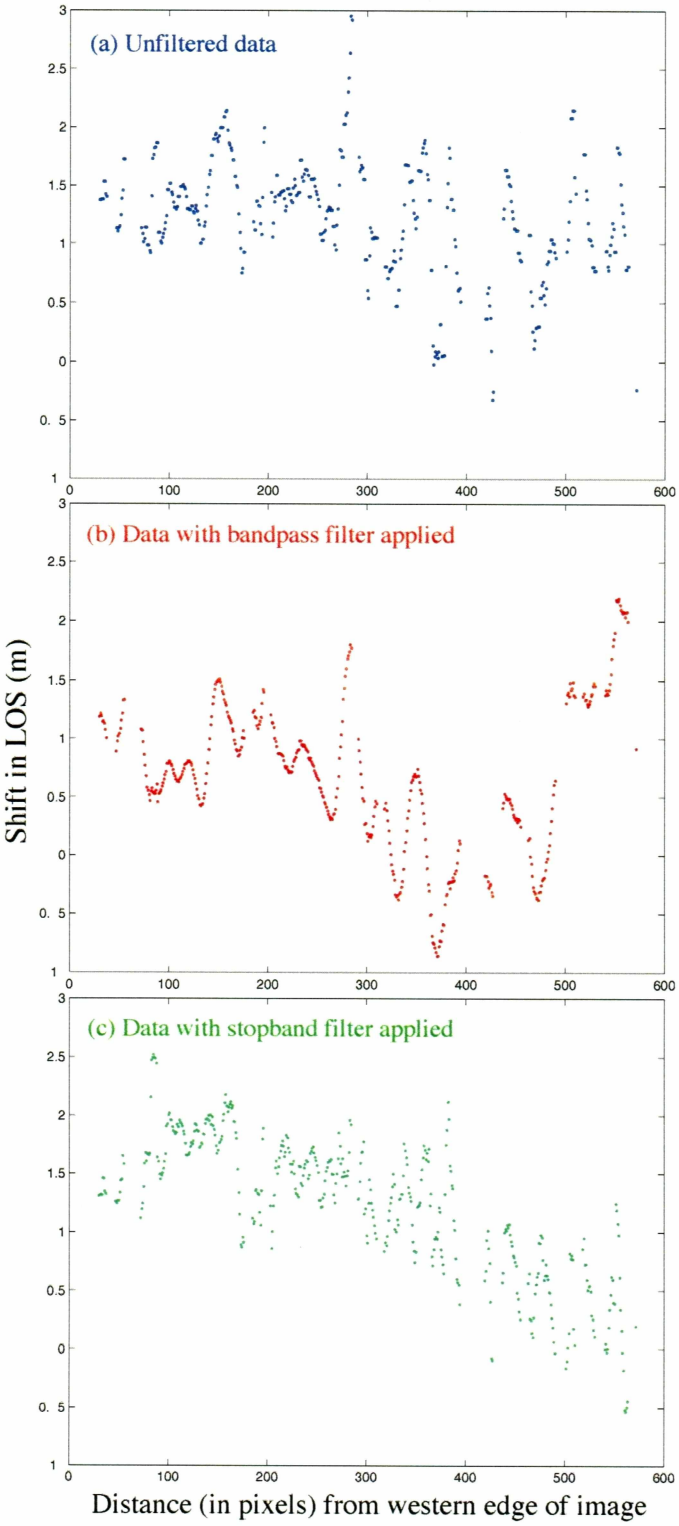

Figure 5.2. Offset values for a sample range line.

meters stood out. To see if this range of wavelengths caused the oscillating signal, I constructed a band pass filter and applied it to a representative range line. Figure 5.2b clearly shows that these wavelengths were responsible. I then created a stop band filter and applied it first to the sample range line (Figure 5.2c) and then filtered the entire offset map line-by-line in the range direction. Any real variations in the data that fell between the wavelengths of 238 and 4,760 meters were removed along with the spurious signal. The scatter seen in Figure 5.2c shows that the stop band filter did not remove all the of noise, but to reduce the possibility of removing additional real signal I did not apply further noise reduction filters.

5.5 Comparison to GPS points

The high density of GPS sites along the Richardson and Denali Highways provided the opportunity to directly compare the GPS measurements and the speckle tracking offsets. Forty-five GPS sites fell within the area of my image, but *Hreinsdóttir* [2005] determined that two of the measurements were unreliable because of their location within a zone of distributed brittle deformation near the fault. I excluded these two points and then projected the other 43 measurements into LOS displacements using the appropriate look vector for each point's location. After locating the corresponding offset pixels, I calculated the offset-GPS residuals. A map of these residuals (Figure 5.3a) revealed a trend of more negative residuals toward the north, indicating that the SAR data contained a ramp. Ramps due to orbit errors and long-wavelength variations in the atmospheric path delays are a very common occurrence in SAR data, so this was not a surprising result. To characterize the ramp, I used the equation

$$\text{Ramp(easting,northing)} = a + b*\text{easting} + c*\text{northing}.$$

I first needed to solve for parameters a, b, and c. Each of the residuals is an estimate of the ramp value at location (easting, northing), so I wrote a simple matrix equation relating the parameters to the residuals. If m is a column vector containing the three parameters, d is the vector of the residuals, and G is a matrix of the form

G(i, :) = [1 easting(i) northing(i)], then

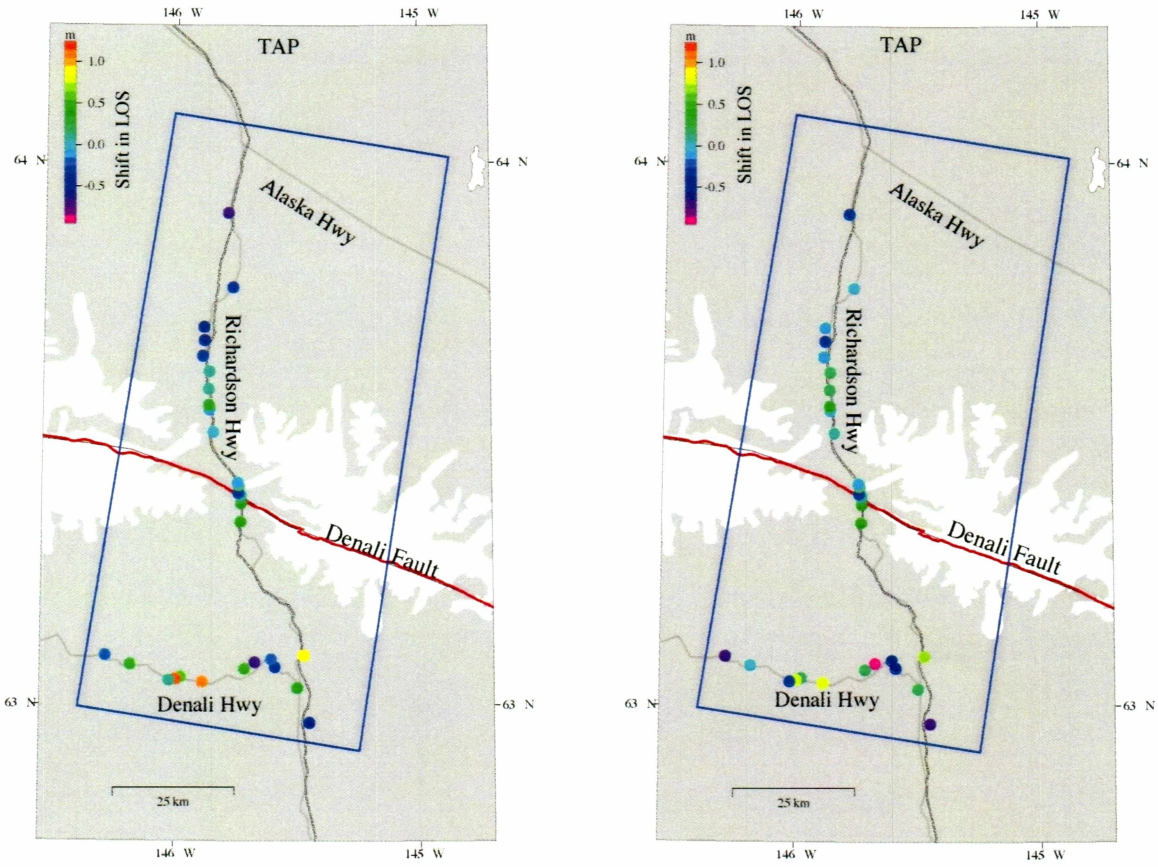

(a) Before ramp removal

(b) After ramp removal

Figure 5.3. Maps of speckle tracking data - GPS data residuals. Colored dots indicate the location and magnitude of the residuals. The blue box shows the area covered by the speckle tracking data and the red line traces the rupture of the Denali Fault earthquake [*Haeussler et al.*, 2004]. Roads and the Trans-Alaska Pipeline (TAP) are shown for reference.

$$d = G*m.$$

A standard least squares inverse was used to estimate m. After calculating and applying the ramp correction at each offset pixel, I again found the offset-GPS residuals. This time, the map (Figure 5.3b) showed a more even distribution of residual values. Since the GPS measurements have a much higher precision than the speckle tracking offset data, the GPS data can be treated as true displacements and used to estimate uncertainty values for the offsets. I found the root mean square of the de-ramped residuals and took this value, about 0.4 meters, to represent the accuracy of the offset data.

6 Coseismic Displacements Determined from Offsets

6.1 Offset Map

Figure 6.1 shows the final filtered offset map. Visible banding is an artifact of filtering. In general, the offsets display a deformation pattern consistent with right-lateral strike-slip motion. As the satellite was flying in a southerly direction, the positive shifts north of the fault indicate movement to the east (towards the satellite) while the negative shifts south of the fault reveal motion to the west (away from the satellite). The most obvious feature of the offset map is the sharp demarcation between the sense of motion on the north and south sides of the fault. This clear boundary is nearly indistinguishable from the mapped surface rupture, supporting previous findings that speckle tracking can be used to locate the fault rupture if it is not known [e.g., *Peltzer et al.*,1999]. West of the Trans-Alaska Pipeline, the offset values near the fault remain fairly constant in magnitude. The maximum offsets on both the north and south sides of the fault occur east of the pipeline. These peak values reach ~ 3 meters of LOS displacement north of the fault and ~ 2 meters south the fault. Roughly translated from the LOS reference frame, these amounts correspond to about 4.2 meters of lateral displacement on the north side and about 2.8 meters of lateral displacement on the south side. Offset values die off to zero towards the north and south edges of the image. In order to investigate the magnitude and distribution of slip along the rupture, I focus my attention on two sub-regions of the offset map.

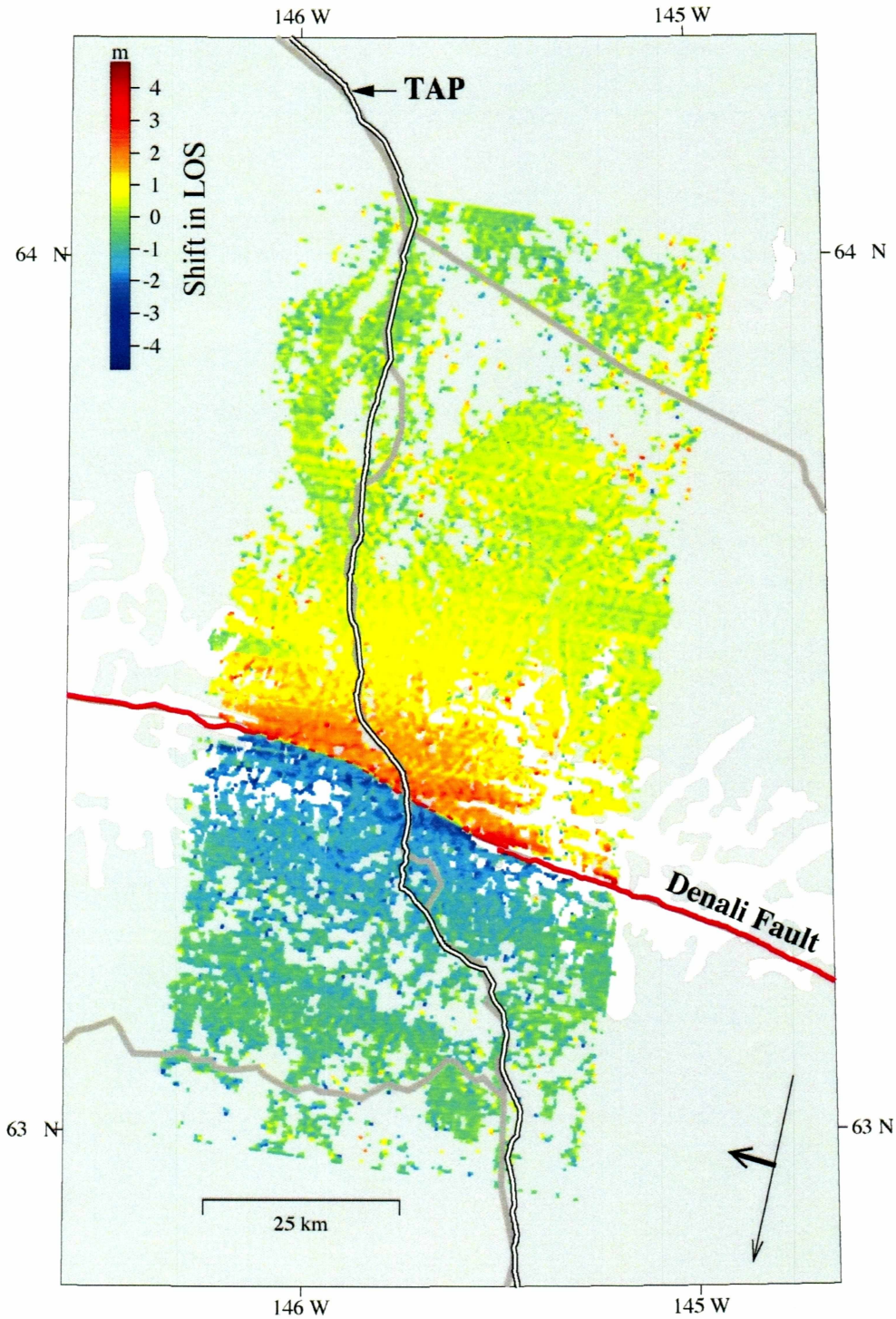

Figure 6.1. Filtered offset map. The earthquake rupture (red line) is taken from *Haeussler et al.* 2004. Roads and the Trans-Alaska Pipeline (TAP) are shown for

reference. The thin arrow shows the direction of the satellite's flight path while the thick arrow indicates the look direction.

6.2 Richardson Highway – Trans-Alaska Pipeline Profile

To gain a better sense of the magnitude of displacement across the fault, I took a cross-strike profile of the offset data centered on the fault-pipeline intersection (Figure 6.2a). I chose this origin point for two main reasons. First of all, that region of the image has fairly continuous data unlike areas to either side that contain significant data gaps near the fault. Secondly, the Richardson Highway corridor boasts a dense network of GPS sites, making comparisons between data sets fairly simple.

The local strike of the Denali fault in this region is about 118°, giving a profile azimuth of 28° [S. Hreinsdóttir, pers. comm. 2003]. To construct the profile, I selected all data points within 500 meters of the azimuth line and projected them onto a single line (Figure 6.2b). During the initial processing, the data was averaged across the fault, resulting in offset values that did not display the real displacement. I found that the averaging affected data located less than 1,200 meters from the fault, so I excluded these offsets from the profile. Overall, the profile shows the decaying curves typical of right-lateral strike-slip motion. On the south side of the fault, the data do not extend far enough for the displacements to die off to zero, but the north side shows that the displacements approach zero by the edge of the offset map at about 80 kilometers. The peak-to-peak displacement in LOS across the fault is about 4 meters. This roughly translates to approximately 6 meters of right-lateral slip. For a better idea of the lateral slip, I compared the speckle tracking data to predictions from the slip model of *Hreinsdóttir* [2005] that were transformed into LOS displacements. The model, which gives a slip value of 5.91 meters at the fault-pipeline junction, has very good resolution at this location because of the large number of GPS sites along the Richardson Highway near the fault crossing. In general, the model shows good agreement with the offset data, particularly near the fault. Farther from the fault, the model tends to display lower LOS displacement values than the speckle tracking data. This could be due to the lack of GPS

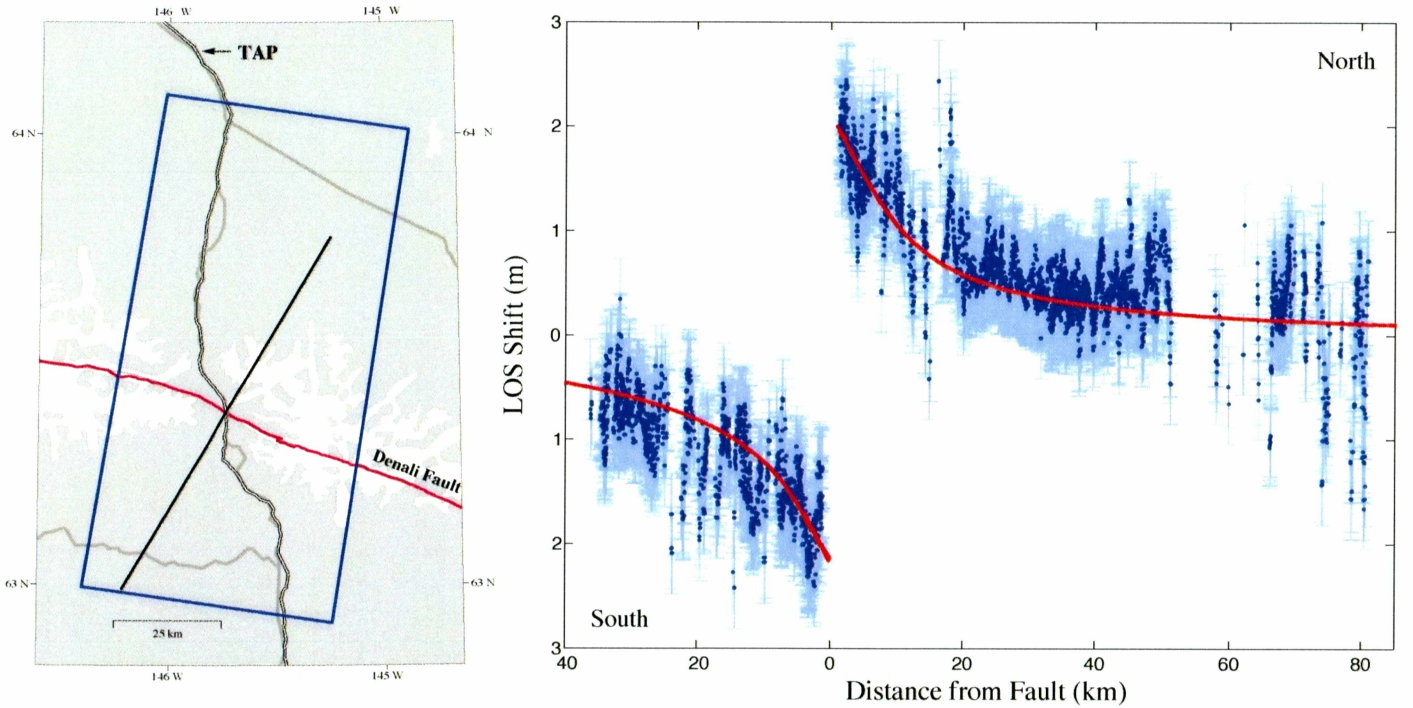

Figure 6.2. Richardson Highway profile. In the location map (left), the black line shows the plane of the profile and the blue box marks the boundaries of the speckle tracking scene. The earthquake rupture [*Haeussler et al.*, 2004] is drawn in red. The Trans-Alaska Pipeline (TAP) is shown for reference. In the data profile (right), blue dots represent the offset values, light blue lines show the error estimates for the offsets, and the red lines are predictions from the model of *Hreinsdóttir* [2005].

sites in these areas (far from the fault, the profile is located well to east of the highway) and correspondingly lower model resolution.

6.3 Along-strike Profiles

Variations in slip along the strike of the fault can indicate changes in fault structure at depth. To examine how displacement changes along the rupture length of the Denali Fault earthquake, I constructed an along-strike profile from the speckle tracking offset map data (Figure 6.3). Within the area covered by my radar image, the Denali fault can be divided into three major segments based on average strike: a western section oriented at ~ 106°, a central region with a strike of about 120°, and an eastern portion striking ~ 110° from north. Data within 2,200 meters of the fault were selected for each of the three segments and then combined into a single profile. As with the cross-strike profile, I excluded data points within 1,200 meters of the fault. I eliminated the entire eastern segment because of sparse data and part of the western segment due to the proximity of the image edge and possible associated biases.

The combined profile displays a fair amount of scatter, some of which results from the width of the data swath used and signal noise not removed by the filter. On the north side of the fault, the profile shows an average LOS displacement of about 2 meters. The magnitude of the displacements remains nearly constant from the western edge of the profile to where a dip occurs just west of the pipeline at about 20 kilometers along the profile (Arrow 1 in Figure 6.3). Moving eastward, displacement values resume the average by the pipeline, decrease to a plateau, and then sharply increase near the eastern end of the profile. The southern profile reveals a similar general pattern, except that the average LOS displacement is about 1.75 meters, the initial dip occurs slightly farther eastward at about 23 kilometers along the profile (Arrow 2 in Figure 6.3), and the data trend shows a small decrease towards the eastern edge of the profile. I compared the data profiles with predictions from *Hreinsdóttir* [2005]'s model converted into LOS displacements. Instead of predicting a model displacement for each data point, I calculated values for locations 1,700 meters from the fault to represent an average for the

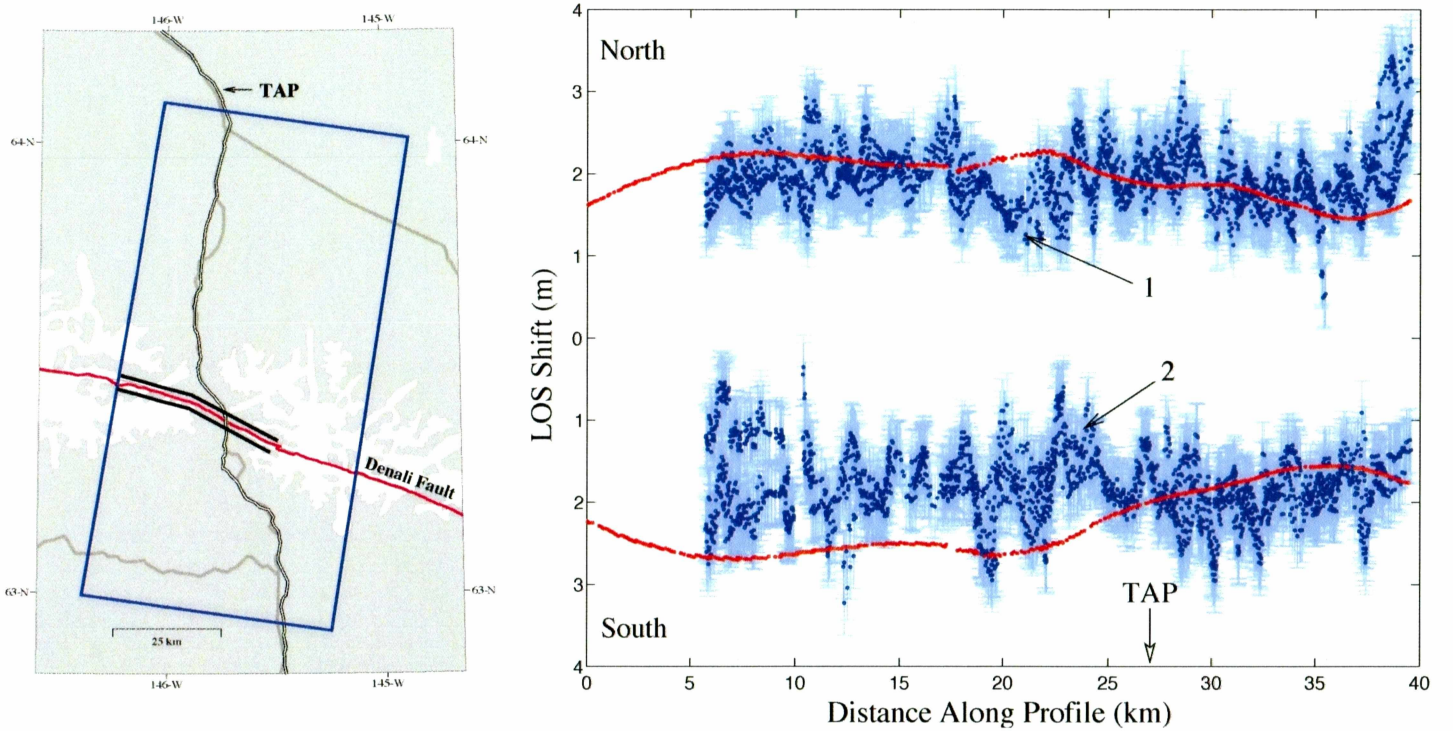

Figure 6.3. Along-strike profiles. In the map (left), the thick black lines show the locations of the along-strike profiles and the blue box marks the boundaries of the SAR scene used. The Trans-Alaska Pipeline (TAP) is included for reference. In the profiles (right), the SAR offsets and their associated error estimates are shown in blue. Predictions from the model of *Hreinsdóttir* [2005] are shown in red.

width of the data swath. Overall, the model values and the data agree best to the north of the fault. Except for a very small area around the 21-kilometer mark, the predictions fall within the uncertainty limits of the data and follow the general data trend. South of the fault, the offsets and model displacements compare favorably east of the Trans-Alaska Pipeline. West of the pipeline, however, the two show very poor agreement south of the fault. Although the model and speckle tracking data follow the same basic trend, a difference of about 0.75 meters exists between the average data value and the model displacements. This could be due to the lack of GPS sites in the area and the consequent lower model resolution, but the corresponding area north of the fault also has a paucity of GPS data. The poor agreement could indicate an aberration in the deformation pattern south of the fault that the GPS model does not capture or could be due to a mis-estimation of the ramp.

6.4 Lateral Slip Estimate

Although the speckle tracking data provide information about deformation patterns around the rupture and displacements on either side of the fault, the LOS geometry can make interpretation of slip and comparison to other datasets difficult. To overcome this problem, I converted the along-strike profile offset data into an estimate of the full lateral displacement. As part of the conversion, I had to account for the fact that the along-strike profile data spanned distances between 1,200 and 2,200 meters from the fault instead of being on the fault trace. To accomplish this, I applied a correction that extrapolated each data point to the location of the fault. I used a simple screw dislocation model [*Savage*, 1990] with a full slip of two meters and a fault depth of 11 kilometers to calculate displacements at distances between 0 and 2,200 meters from the fault. For each of the profile data point locations, I found the corresponding model prediction and took the ratio of it to the model displacement estimate located closest to the fault. Since I chose a full slip of two meters, the maximum displacement on either side of the fault was 1 meter. Consequently, the denominator of the ratios was one, which simplified the calculations. This process resulted in a set of ratios that related the displacement at the fault to

displacements at the profile distances. For example, the ratio of a displacement value located 1,700 meters from the fault (the mean distance for the along-strike profiles) to displacement at the fault is 0.9024 (0.9024 meters/1 meter). Dividing each of the along-strike profile offsets by its appropriate ratio yielded an estimate of displacement at the fault.

The conversion is based on the premise that the displacement in LOS is equal to the dot product of the radar's look vector with the displacement vector (½ u), which in geographic coordinates is:

$$\text{Displacement}_{\text{LOS}} = (l_{east}, l_{north}, l_{up}) \bullet \tfrac{1}{2}\, u.$$

The factor of ½ arises because each side of the fault moves a distance ½ u relative to a remote reference frame. In terms of earthquake displacements, the full slip vector can be broken into

$$u = (\text{ss} \cos\phi\ \hat{e},\ \text{ss} \sin\phi\ \hat{n}\ ,\ \text{dipslip}\ \hat{v})$$

where ss represents strike-slip and ϕ is equal to the average fault strike – 90°. Substituting this expression for the full slip vector into the first equation for displacements north of the fault yields

$$\text{Displacement}_{\text{LOS}} = \tfrac{1}{2}(\text{ss} \cos\phi * l_{east} - \text{ss} \sin\phi * l_{north} + \text{dipslip} * l_{up}).$$

Haeussler et al. [2005] found that, on average,

$$\text{dipslip} = 0.17 * \text{ss}$$

(with the north side up) along the rupture of the Denali fault. Substituting and simplifying,

$$\text{Displacement}_{\text{LOS}} = \tfrac{1}{2}\ \text{ss}(\cos\phi * l_{east} - \sin\phi * l_{north} + 0.17 * l_{up}).$$

Rearranging terms,

$$\text{ss} = \frac{\text{Displacement}_{\text{LOS}}}{\tfrac{1}{2}\ (\cos\phi * l_{east} - \sin\phi * l_{north} + 0.17 * l_{up})}$$

Since the 2002 rupture was north side up, the final equations become

$$\text{North side ss} = \frac{\text{Displacement}_{\text{LOS}}}{\tfrac{1}{2}\ (\cos\phi * l_{east} - \sin\phi * l_{north} + 0.17 * l_{up})}$$

$$\text{South side ss} = \frac{\text{Displacement}_{LOS}}{\tfrac{1}{2}\,(-\cos\phi * l_{east} + \sin\phi * l_{north} - 0.17 * l_{up})}.$$

As discussed earlier, the values for the components of the look vector vary according to the location of the data point. Using the appropriate look vector values and the LOS displacements from the along-strike profiles from the north and south sides of the fault in the above equations produced two estimates of the full lateral slip. I reduced the number of data points by averaging every 50 points (north and south estimates separately), an amount that corresponds to a distance of about 100 meters. As a final step, I found the mean of the two lateral slip estimates.

Figure 6.4 shows the mean slip estimate along with geologic surface slip measurements and lateral slip predictions from the model of *Hreinsdóttir* [2005]. The speckle tracking slip estimate displays variable slip along the fault with an overall average value of about 5 meters. The slip estimate climbs from a minimum of ~ 3.8 meters several kilometers west of the pipeline to a peak of 6.1 meters just east of the pipeline. East of this peak, the data declines into a trough with an average slip of about 5.2 meters. At the pipeline, the speckle tracking data give a slip value of about 5.4 meters. Except for a few points, the speckle tracking estimates are larger than the geologic surface slip measurements. This supports the conclusions of *Haeussler et al.* [2004] and *Hreinsdóttir* [2005] that ground surface conditions in the regions adjacent to the pipeline prevent the geologic offsets from recording the full slip values. Eastward of the 23-kilometer mark, the general shape of the speckle tracking estimate curve and the line predicted by the GPS model agree and nearly all of the model predictions fall within the uncertainty bounds of my data estimates. West of this point, the two estimates compare more poorly, particularly at about 22.5 kilometers from the profile origin where the speckle tracking estimate shows a peak of about 3.8 meters and the model predicts a peak value of nearly 7 meters. This area is west of the Richardson Highway GPS network, so the resolution of the model of *Hreinsdóttir* [2005] may be lower for this region.

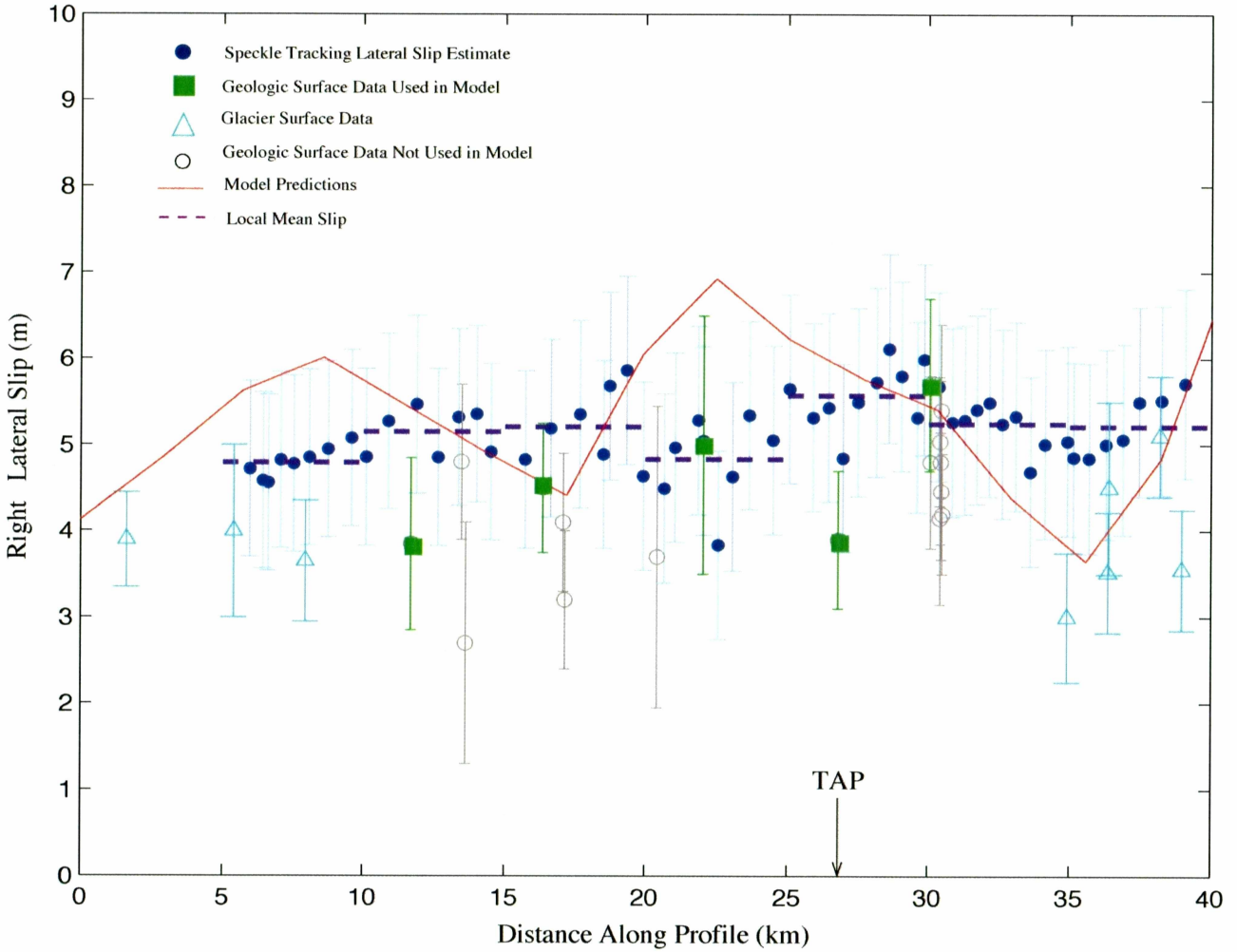

Figure 6.4. Lateral Slip Esitmate Plot. The mean local slip is the mean slip for each 5 km interval. All geologic data is taken from *Haeussler et al.* [2004]. Model predictions are those of *Hreinsdóttir* [2005].

7 3-D Fault Model

7.1 Data

I inverted for the coseismic slip distribution of the Denali Fault earthquake using a combination of the speckle tracking data, GPS measurements, and geologic surface offsets. By adding the speckle tracking data to the GPS and geologic data-derived model of *Hreinsdóttir* [2005], I hope to improve that model in the central section of the Denali Fault earthquake rupture, especially in the areas where GPS data are sparse or non-existent. A model with improved resolution will allow a better estimation of the surface slip and elucidate the slip pattern in a structurally complex region that includes fault bends, stepovers, and splays.

The GPS dataset included measurements from 224 sites. Among the geologic surface offset data, all glacier measurements were excluded because they likely underestimated the total amount of slip [*Hreinsdóttir*, 2005; *Haeussler et al.*, 2004]. In addition, I selected only the largest reliable geologic surface offset within each 3-kilometer segment of the rupture (a length corresponding to the size of model tiles discussed below). This choice was due to a suggestion by P. Haeussler that the largest geologic measurements within a local area are most likely to accurately reflect the true amount of slip. Out of a total of 107 segments, 47 contained reliable geologic surface offset measurements. All of the 47 offsets chosen came from the Denali and Totschunda faults. Details about uncertainties and weighting for the GPS and geologic data can be found in *Hreinsdóttir* [2005].

Although I had reduced the speckle tracking data previously (see section 5.2), the resulting dataset of 710,895 points was still far too large for practical modeling. To reduce the data further, I used a technique known as quadtree decomposition [e.g., *Jónsson et al.*, 2002]. This method divides a gridded image into four quadrants and continues to divide each quadrant into four new quadrants until certain conditions are met. In my case, the division stopped either when the difference between the maximum and minimum values in a quadrant fell below a specified threshold or when the quadrant

box reached a minimum size, whichever occurred first. This process results in a large number of data points in areas with high deformation gradients and a small number of data points in areas with little or no deformation.

In my quadtree decomposition, I set the threshold value to 0.4 meters, the uncertainty estimate found for the speckle tracking data (see section 5.5) and chose a minimum box size of 1 kilometer, double the resolution produced by the cross-correlation procedure (see section 5.1). After performing the decomposition, I visually inspected the reduced data for obvious outliers and removed 31 points. The final dataset had a total of 1,879 points (Figure 7.1).

7.2 Fault Model

I adopted the fault model geometry used by *Hreinsdóttir* [2005], which consisted of an 11-plane approximation to the Susitna Glacier, Denali, and Totschunda faults with each plane subdivided into 3-kilometer by 3-kilometer tiles (Table 7.1). The model Susitna Glacier fault had two planes: an upper plane that intersects the ground surface at about the observed surface rupture and has a dip in agreement with field measurements, and a lower plane whose base intersects the Denali fault and has a dip consistent with the first motion focal mechanism. Seven planes approximate the Denali fault between the down-dip end of the Susitna Glacier fault and the Denali-Totschunda fault junction, limits that agree with geodetic, seismic, and geologic observations [*Hreinsdóttir et al.*, 2003; *Haeussler et al.*, 2004; *Ratchkovski et al.*, 2004]. All of the Denali planes as well as the two Totschunda fault planes have a vertical dip and they extended from the surface to a depth of 18 kilometers. *Hreinsdóttir* [2005] discussed the justification for this model geometry in detail.

7.3 Inversion Method

I closely followed the inversion method of *Hreinsdóttir* [2005] and details not discussed in the following summary can be found there. To estimate the coseismic slip value for each model fault tile, I utilized the damped least-squares method of *Price and Bürgmann*

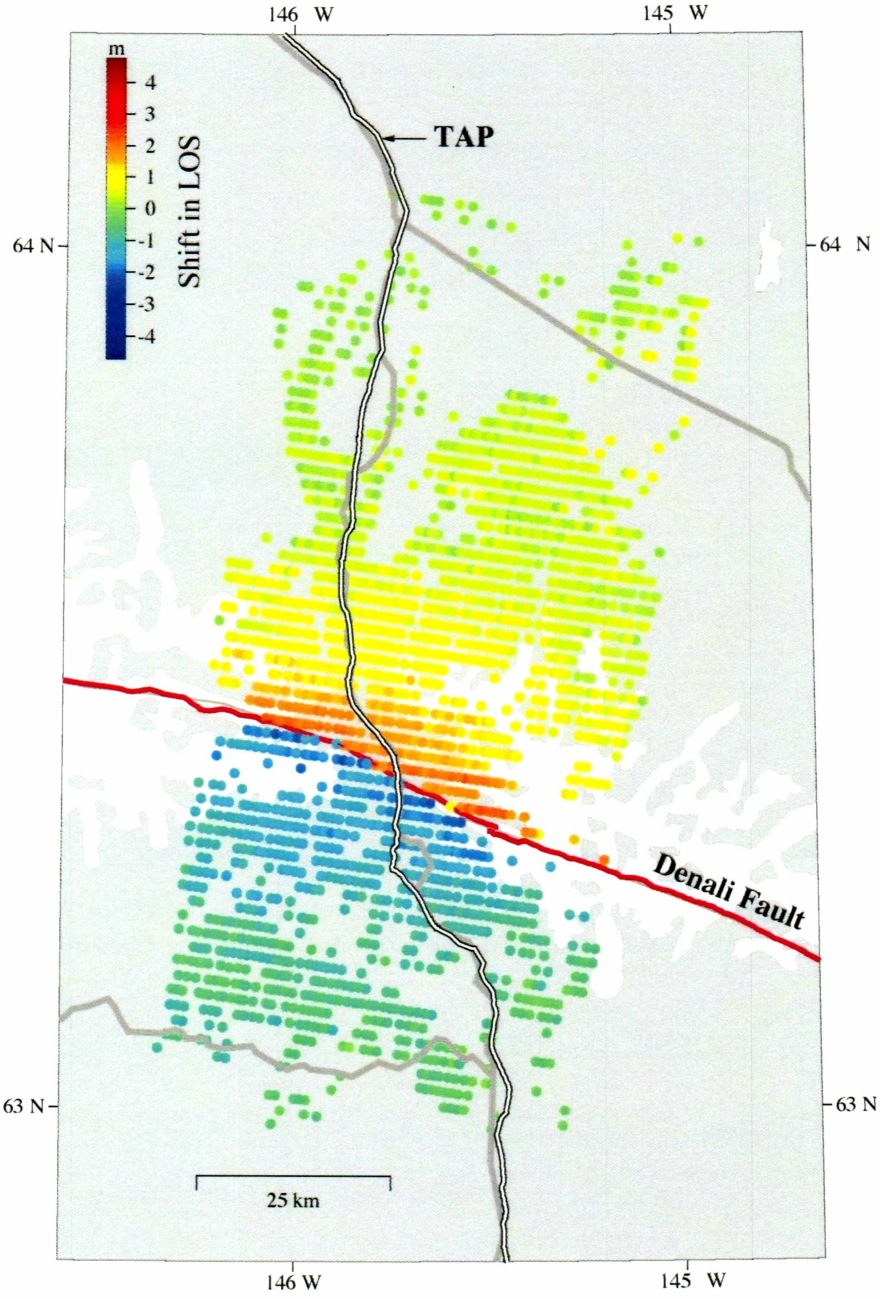

Figure 7.1. Speckle tracking data reduced by quadtree decomposition. Each point shows the the average data value in a quadtree box and is located at the center point of that quadtree box. The Trans-Alaska Pipeline is shown for reference.

Table 7.1. Model Fault Geometry

Fault	Strike (°)	Dip (°)	Lat. Start (°N)	Lat. End (°N)	Long. Start (°W)	Long. End (°W)	Min. Depth (km)	Max. Depth (km)
Susitna Glacier								
Upper Plane	81	19	63.4	63.46	147.7	147.05	0	2
Lower Plane	81	48	63.45	63.53	147.7	147.07	2	8.6
Denali								
Plane 1	81	90	63.5	63.54	147.75	147.22	0	18
Plane 2	98	90	63.54	63.47	147.22	146.23	0	18
Plane 3	106	90	63.47	63.43	146.23	145.89	0	18
Plane 4	120	90	63.43	63.34	145.89	145.51	0	18
Plane 5	110	90	63.34	63.23	145.51	144.92	0	18
Plane 6	116	90	63.23	63.07	144.92	144.22	0	18
Plane 7	119	90	63.07	62.84	144.22	143.34	0	18
Totschunda								
Plane 1	151	90	62.84	62.67	143.34	143.16	0	18
Plane 2	137	90	62.67	62.34	143.16	142.53	0	18

[2002]. For the GPS, geologic, and speckle tracking data, I calculated the Green's functions, $\mathbf{G_{GPS}}$, $\mathbf{G_{geooffset}}$, and $\mathbf{G_{speckle}}$, to relate slip s to surface displacement d by

$$\begin{bmatrix} d_{\text{GPS}} \\ d_{\text{geooffset}} \\ d_{\text{speckle}} \end{bmatrix} = \begin{bmatrix} \mathbf{G}_{\text{GPS}} \\ \mathbf{G}_{\text{geooffset}} \\ \mathbf{G}_{\text{speckle}} \end{bmatrix} [s].$$

Green's functions are the displacements at each GPS site, geologic offset position, or SAR quadtree point location that would result from 1 meter of slip on each model fault tile assuming an elastic half-space and a Poisson's ratio of 0.25 [*Okada*, 1985], and represent the response of the earth to a unit input. For $\mathbf{G_{speckle}}$, I computed the three-dimensional displacements at each data location and then took the dot product with the look vector to obtain the displacement in the radar's LOS. In the case of the geologic data, the 47 surface measurements were directly related to slip on their corresponding model tiles so that $\mathbf{G_{geooffset}}$ was equal to $\mathbf{I}$, the identity matrix.

In the inversion, I used 2,642 data (1,879 single-component speckle tracking data, 221 three-component GPS data, 3 two-component EDM-GPS data, and 47 two-component geologic surface measurements) to estimate 1,394 model parameters (strike-slip and dip-slip on 697 tiles) as well as 22 parameters that put additional constraints on the surface tiles of the Susitna Glacier fault. The bounded variable least-squares algorithm of *Stark and Parker* [1995] was used to constrain slip on each tile. To agree with geological measurements [*Haeussler et al.*, 2004; *Crone et al.*, 2004], slip was restricted to right-lateral strike-slip and north-side-up dip-slip. The Denali and Totschunda faults had an imposed upper bound of 3 meters of dip-slip, as in *Hreinsdóttir* [2005].

To stabilize the inversion, I used discrete Laplacian smoothing between the model tiles. Choosing an appropriate smoothing factor, β, will minimize both the weighted residual sum of squares (WRSS) and the roughness of the model given by

$$\mathrm{F}(misfit, roughness) = \underbrace{\left\|\mathbf{W}(\mathbf{G}s - d)\right\|^2}_{Misfit} + \beta^2 \underbrace{\left\|\mathbf{L}s\right\|^2}_{Roughness}$$

where $\mathbf{L}$ is the Laplacian operator and $\mathbf{W}^T\mathbf{W} = \boldsymbol{\Sigma}^{-1}$ and $\boldsymbol{\Sigma}$ is the data covariance matrix. Changing the smoothing factor changes the model's WRSS and roughness values, so generating a number of models with different smoothing factors allows the construction of a tradeoff curve between misfit and roughness (Figure 7.2). Selecting the optimal smoothing factor from the tradeoff curve is highly subjective, so *Hreinsdóttir* [2005] also used the method of Weighted Cross-Validation Sum of Squares [*Matthews and Segall*, 1993] to provide an estimate of the best value for the smoothing factor. However, this technique is not practical for the present model due to the large number of data involved and because the SAR data are spatially correlated with themselves. Instead, I compared the tradeoff curve for the present model (Figure 7.2) with the WRSS versus roughness curve of *Hreinsdóttir* [2005] to determine if I could justify adopting the optimal smoothing factor used in that study. Given the great similarity between the two curves, I decided that *Hreinsdóttir's* [2005] values were valid for my model as well and considered smoothing factors between 2.5 and 7 km^2/m to be reasonable choices with $\beta = 4$ km^2/m being the optimal value. Figure 7.3 shows the range of reasonable models. The three models show similar results: between 3 and 8 meters of dip-slip, with about 4.5 meters at the epicenter, on the Susitna Glacier fault; variable, mostly right-lateral strike-slip motion along the Denali fault with a peak of 9-11 meters of slip west of the Denali-Totschunda fault junction; and shallow, right-lateral slip of between 1-4 meters on the Totschunda fault.

The addition of the speckle tracking data to the inversion did not significantly change the misfit between the GPS data and the model predictions. The WRSS for the preferred GPS-derived model (1,250.5) is virtually identical to the WRSS calculated for the GPS portion of the combined speckle tracking/GPS/geologic data model (1,249.9). When I compared the residuals between the GPS model and data to the residuals between the combined model and the GPS data, I found that only four GPS sites showed differences of more than 2 centimeters. These four sites (three along the Pipeline corridor and one on the Black Rapids Glacier) do have higher than average uncertainty

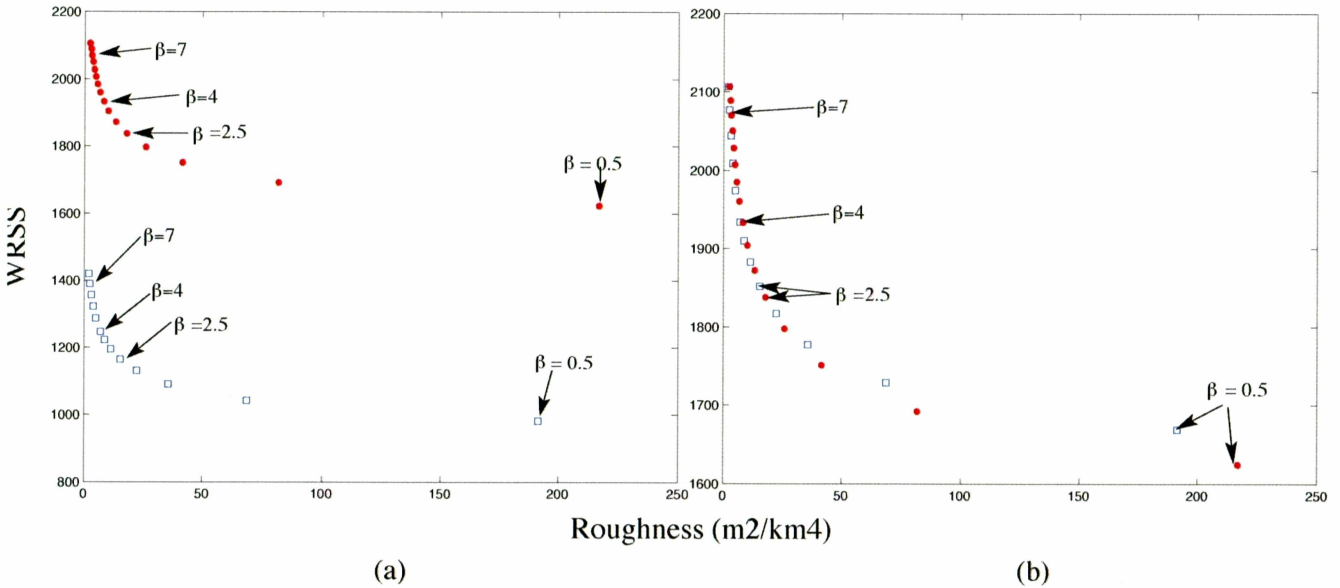

Figure 7.2. Tradeoff curves. (a). Comparison of tradeoff curves for the model of this study (top, red dots) and the model of *Hreinsdóttir* [2005] (bottom, blue squares). Labels of data points give the smoothing factor in km^2/m. WRSS is weighted residual sum of squares. (b). Curves shifted so that the top data point of each ($\beta = 9$) are aligned with each other. $\beta = 4$ gives the optimal smoothing.

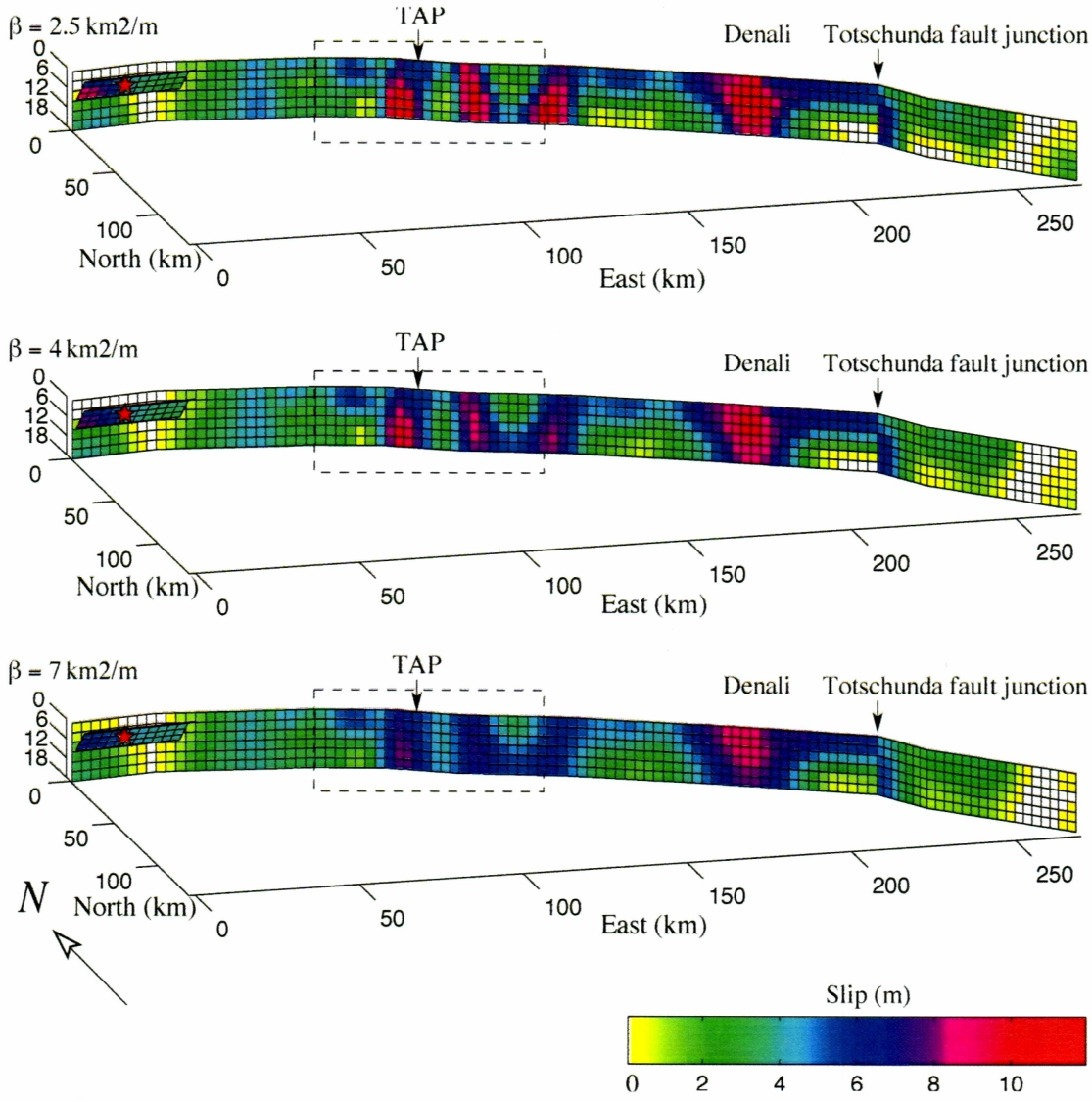

Figure 7.3. Range of reasonable coseismic slip models. The vertical axis shows depth while the horizontal axes show kilometerws north and east of the fault model's origin. The Trans-Alaska Pipeline (TAP) and the Denali-Totschunda fault junction are labeled for reference. The epicenter of the Denali Fault earthquake is marked by the red star. The dashed box indicates the region with speckle tracking coverage.

estimates. The average misfit between the combined model and the speckle tracking data is about 23 centimeters, a value well below the speckle tracking uncertainty estimate of 40 centimeters. These small misfits indicate that all of the datasets used in the inversion are highly compatible with each other.

7.4 Preferred Coseismic Slip Distribution Model

The combined coseismic slip model with $\beta = 4$ km^2/m (Figures 7.4 and 7.5) shows a highly variable slip distribution along the three faults and has a total moment of 6.85×10^{20} N•m (assuming a modulus of rigidity of 30 GPa), which corresponds to an M_w 7.89 earthquake. On the Susitna Glacier fault, the model displays an average of about 4.5 meters of dip-slip motion. Absence of GPS and speckle tracking data near the fault requires the model to rely on geologic surface data and prevents finer resolution of slip along the fault. This fact, along with the lack of geologic evidence for significant lateral slip [*Crone et al.*, 2004], leads me to believe that the strike-slip motion seen in the model is an artifact. Strike-slip on the Susitna Glacier fault and the Denali fault are probably indistinguishable from each other given the data distribution. Modeled slip along the Denali fault is overwhelmingly right-lateral strike-slip and increases, on average, from west to east. At the epicenter, the model shows very low strike-slip values below 6 kilometers and no surface slip. This is in agreement with the geologic observations of no significant surface slip along the Denali fault in this area [*Haeussler et al.*, 2004]. Between 11 and 60 kilometers east of the epicenter, the model displays strike-slip motion of ~ 0-4 meters, with a median value of about 3 meters. There is also significant dip-slip of up to 3 meters in this region. From 60-140 kilometers east of the epicenter, the model predicts three major patches of strike-slip motion. Centered at about 80, 106, and 128 kilometers east of the epicenter, the three patches reach maximum slip values of 8.5-10 meters at depths of between 9 and 15 kilometers. This segment of the model displays a striking lack of dip-slip motion compared to segments to the east and west (Figure 7.5). The segment between 136 and 160 kilometers east of the epicenter shows overall lower slip estimates, with the maximum values at the surface, as well a moderate amount of

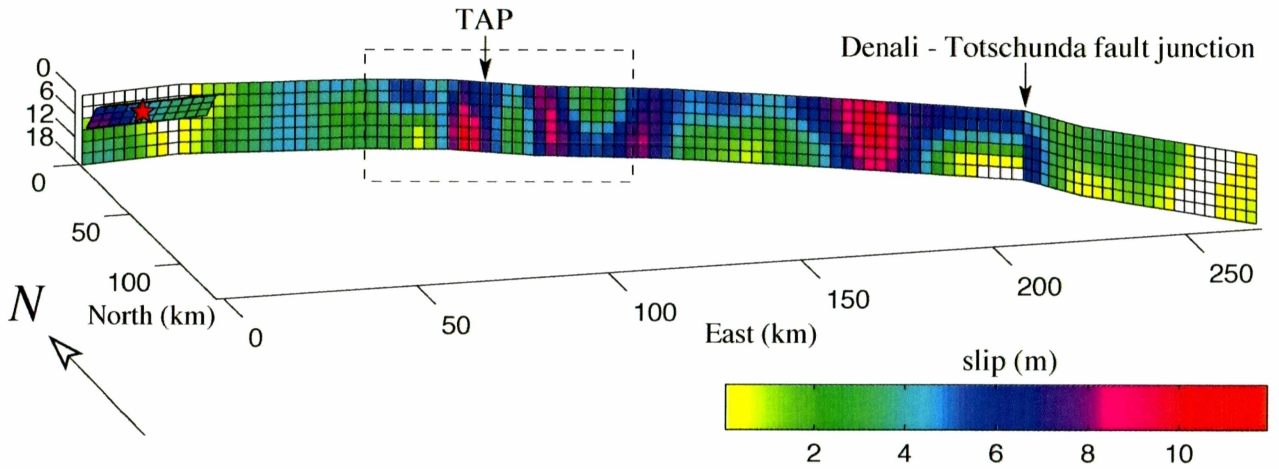

Figure 7.4. Preferred coseismic slip distribution model. The vertical axis shows depth in kilometers while the horizontal axes show the distance north and east of the fault model's origin. The Trans-Alaska Pipeline (TAP) and the Denali-Totschunda fault junction are shown for reference. The dashed box indicates the extent of the speckle tracking scene.

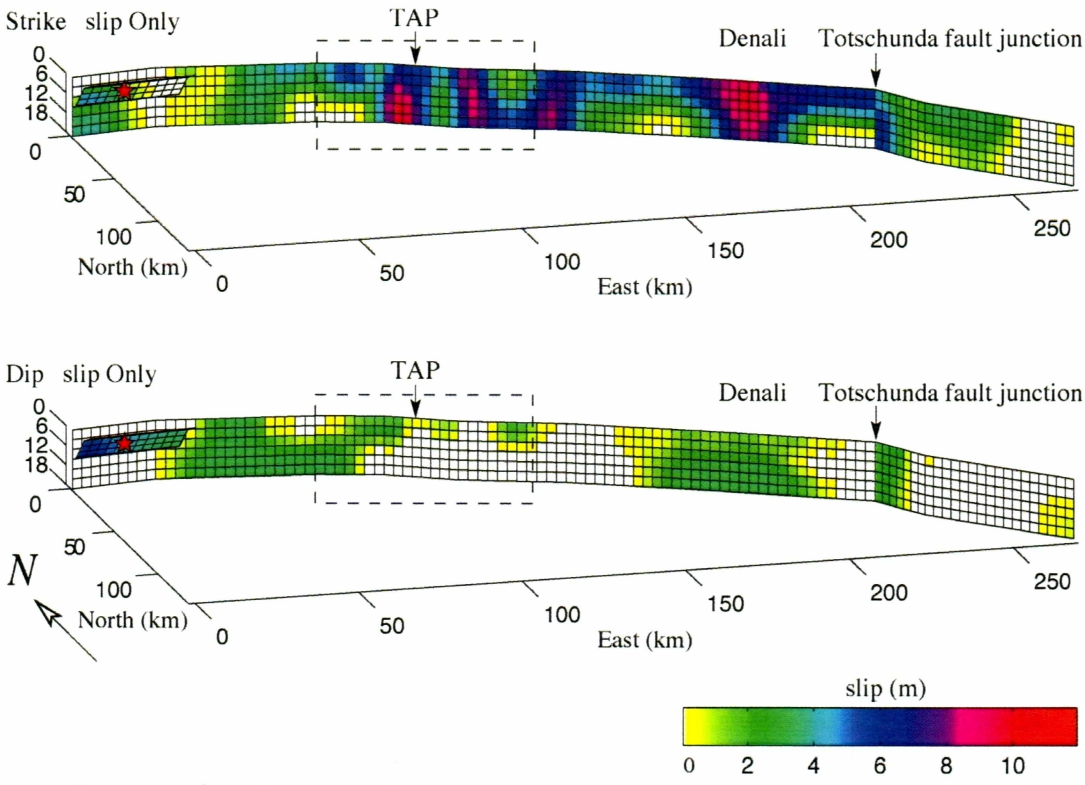

Figure 7.5. Preferred coseismic model separated into strike-slip and dip-slip. The vertical axis shows depth in kilometers while the horizontal axes show distance north and east of the fault model's origin. The Trans-Alaska Pipeline (TAP) and the Denali-Totschunda fault junction are shown for reference. The epicenter of the Denali Fault earthquake is marked by the red star. The dashed box shows the area covered by the speckle tracking data.

dip-slip motion. The largest slip patch, in terms of both magnitude and spatial extent, occurs between 160 and 186 kilometers east of the epicenter. This patch displays slip estimates of over ten meters at the surface and shallow depths, a result that corresponds to the largest geologic slip measurement of 8.8 meters [*Haeussler et al.*, 2004]. A significant dip-slip component is also predicted for the area. Along the Totschunda fault, the model predicts relatively low right-lateral slip of between 1 and 3 meters concentrated at shallow depths.

After projecting the combined model predictions into the LOS reference frame, I compared them to the along-strike speckle tracking data profiles discussed in section 6.2 (Figure 7.6). In general, the combined model follows the speckle tracking data trend more closely than the GPS-derived model of *Hreinsdóttir* [2005]. At the Trans-Alaska Pipeline, the two models coincide, which isn't a surprising result since the GPS model is extremely well resolved there. Away from the pipeline, the inclusion of the speckle tracking data provided additional constraints to the GPS model, particularly in the regions west of 23 kilometers and east of 33 kilometers from the profile origin.

I also added predictions from my model to the lateral slip estimate plot discussed in section 6.3 (Figure 7.7). Once again, the two models agree extremely well in the area of the Trans-Alaska Pipeline while my model fits the data better at other locations. In particular, there is good agreement between the speckle tracking lateral slip estimate and my model to the east of the pipeline. The exception is the drop in the combined model slip prediction at about 15 kilometers from the origin. Here there is a greater discrepancy between the speckle tracking slip estimate and my model than between the estimate and the GPS model. Based on its shape, this is probably a result of the smoothing constraint used in the model. The goal of the inversion method is to minimize the second derivative of the sum of squares of the residuals between the data and the model estimate. Broad, shallow curves will have lower second derivative values than sharp peaks that change slope abruptly. The smoothing factor acts to give the model estimates the lowest possible second derivative values. The fewer data constraints an area contains, the more influence the smoothing factor will have. In this case, the broad, deep dip displayed by the

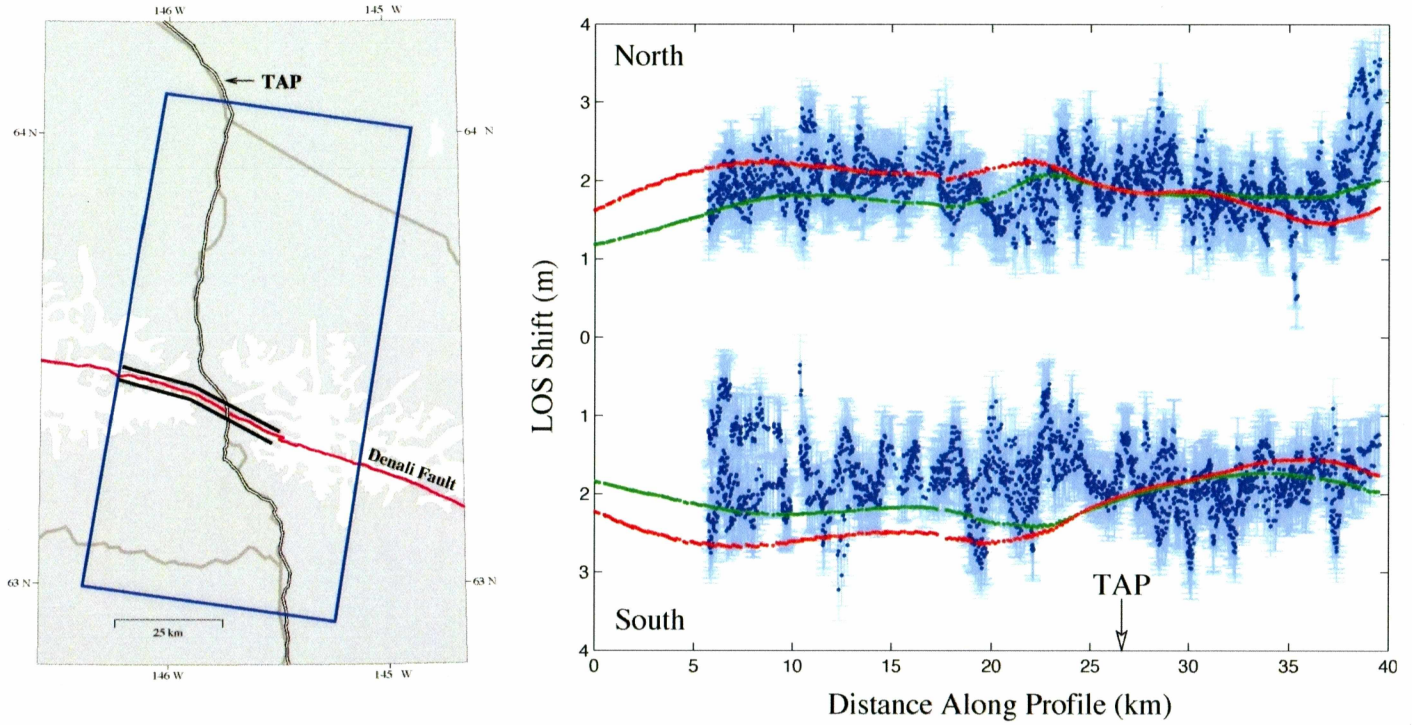

Figure 7.6. Along-strike profiles with model predictions. In the map (left), the thick black lines show the location of the along-strike profiles and the blue box marks the boundaries of the SAR scene used. The Trans-Alaska Pipeline (TAP) is included for reference. The thick red line denotes the trace of the earthquake rupture. In the data profiles (right), the SAR offsets and their associated error estimates are shown in blue. Predictions from the model of *Hreinsdóttir* [2005] are shown in red while estimates from this study's model are shown in green.

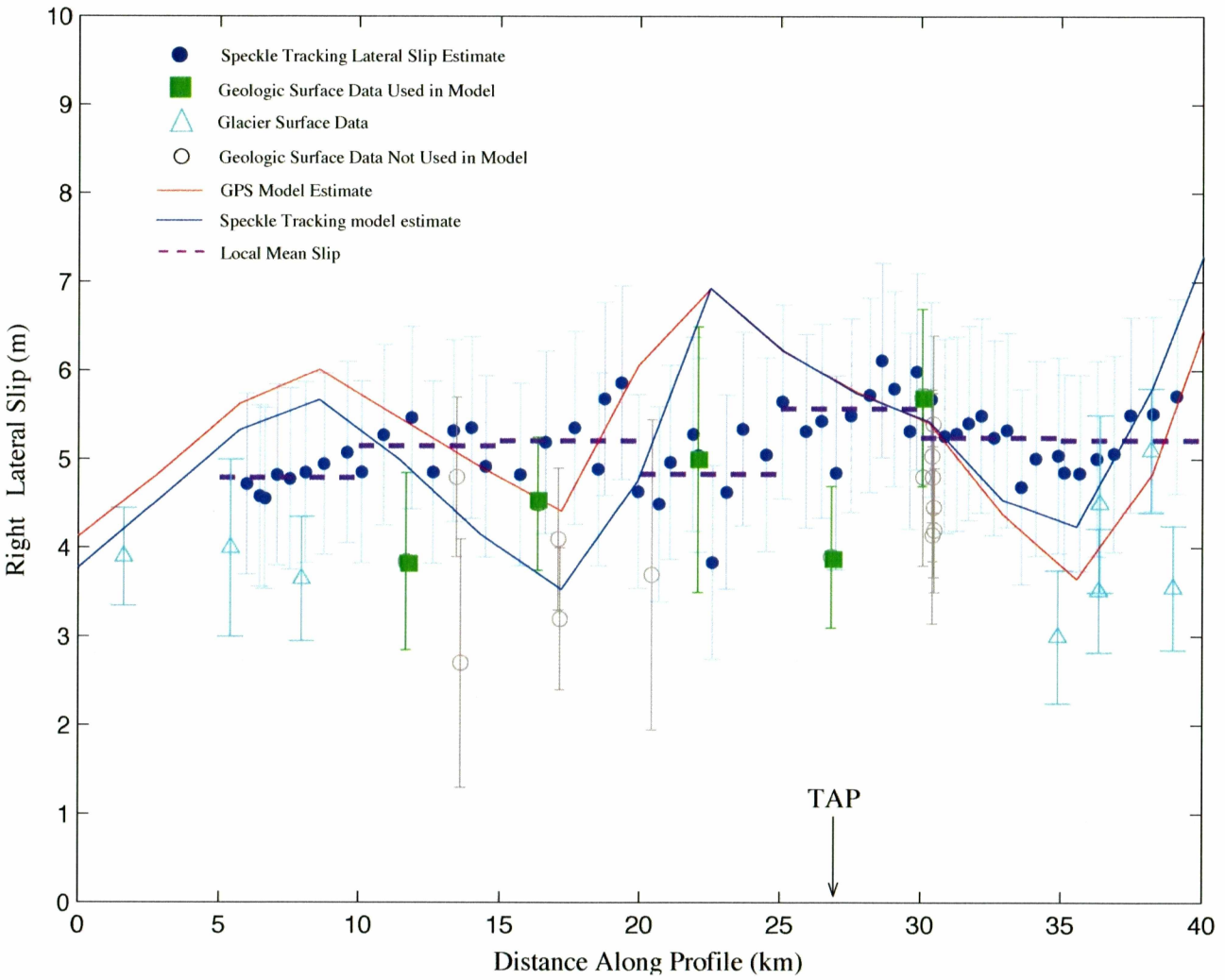

Figure 7.7. Lateral slip estimate with combined model predictions. The local mean slip is the mean slip for each 5 km interval. Reference for the geologic data and the GPS model are the same as those of Figure 6.4.

combined model results in a lower second derivative value than if the model had changed course to intersect the other speckle tracking data.

Figure 7.8 shows a comparison between the geologic surface data and the slip predictions of my model for the Denali and Totschunda faults. Overall, there is very good agreement between the model and the geologic data for both lateral slip and dip-slip. As mentioned in section 7.3, dip-slip motion on all model tiles was restricted to north-side up slip. Given the good fit between the model and the data, along with the fact that the vast majority of the geologic data show north-side-up slip, this assumption seems to be justified. The good fit also offers further evidence of the compatibility of the datasets.

8 Discussion

As Figure 6.4 shows, the largest geologic surface offsets (those used in the inversion model) agree in general with the speckle tracking slip estimates and are, on average, within 1 sigma of the mean slip estimate. With the exception of the large cluster of data just east of the pipeline, the other geologic surface offsets are lower than the speckle tracking estimates and have an average deviation of 1.44 sigma below the local mean. As mentioned in section 7.1, P. Haeussler suggested that the largest geologic surface offset measurements within a local area most accurately represent the true amount of slip. The above comparison of the speckle tracking lateral slip estimates to the geologic measurements provides further evidence that this suggestion is correct. Since estimating the lateral slip from speckle tracking data requires assuming the ratio of vertical to horizontal slip, this method cannot replace geologic field observations. However, the estimates are useful complements to the geologic surface offsets, extending their coverage and allowing reliable interpolation between them.

Overall, the speckle tracking data compare favorably with the GPS measurements. In areas with a dense network of GPS sites, such as the Trans-Alaska Pipeline/Richardson Highway corridor, the GPS-derived slip model of *Hreinsdóttir* [2005] shows extremely good agreement with the speckle tracking data (Figure 6.2). The largest differences

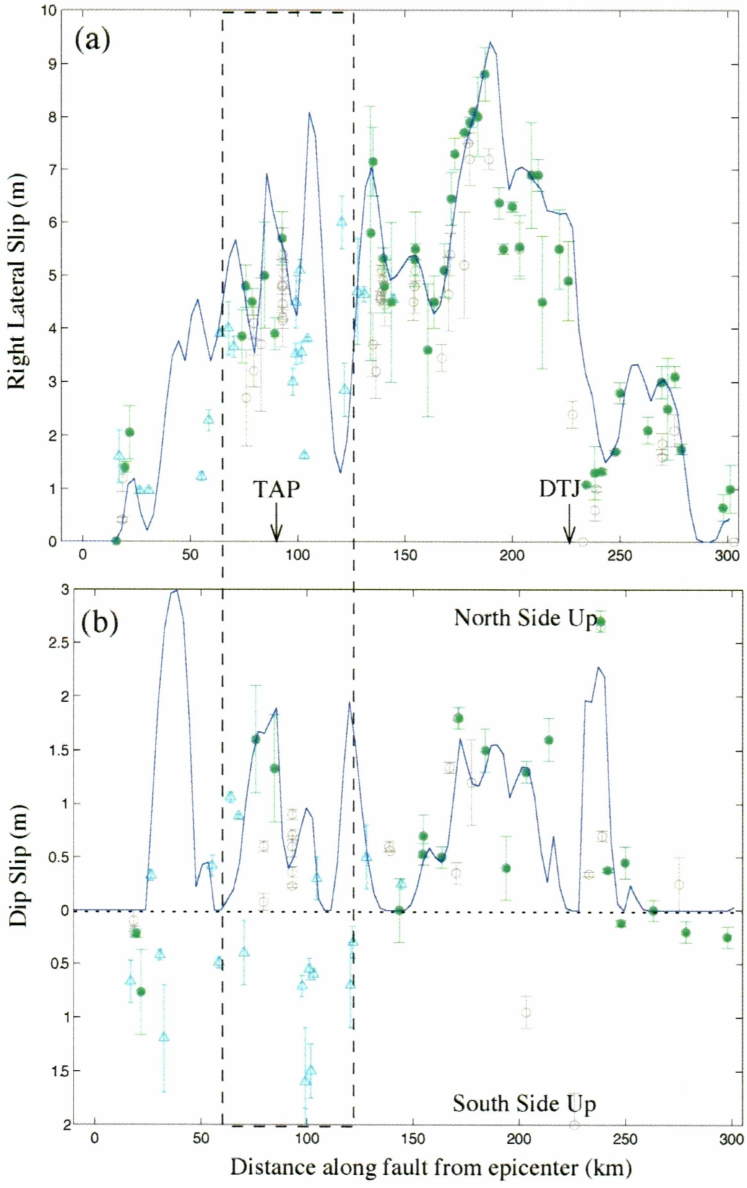

Figure 7.8. Comparison between combined model and geological data. (a). Right-lateral slip plot. (b). Dip-slip plot. Hollow blue triangles represent glacier offset data, hollow grey circles show non-glacier geologic offsets not used in the inversion model, and solid green circles are the geologic surface offsets used in the model. All geologic data are from *Haeussler et al.* [2004]. The blue line is the estimate of the combined model. The Trans-Alaska Pipeline (TAP) and the Denali-Totschunda fault junction (DTJ) are shown for reference. The dashed box shows the region covered by the speckle tracking data.

between the model and my data occur in regions with few or no GPS sites, where the resolution of the GPS-derived model is expected to be lower. These results imply that despite a large level of uncertainty relative to the GPS data, the speckle tracking data can provide a robust estimate of the coseismic displacements assuming the displacements are large compared to the speckle tracking uncertainty. This means that displacements can be obtained from remote regions away from the heavily road-based GPS networks, providing a more complete picture of the deformation caused by the Denali Fault earthquake.

Since this study's model and the model of *Hreinsdóttir* [2005] share a model fault geometry, GPS data, geologic surface data, and an inversion method, the two slip distributions have a number of similarities. The geodetic moments, 6.81×10^{20} N•m for the GPS/geologic data model and 6.85×10^{20} N•m for the combined model, are nearly identical. Outside of the area covered by the speckle tracking image, the slip distributions do not significantly vary from each other. Within that area, however, the two models display considerable differences (Figure 8.1 and Figure 8.2). In Figure 8.2, a positive difference indicates that the combined model predicts a larger amount of slip than the GPS/geologic model. The strike-slip plot shows two large areas of positive differences of 1 to 2+ meters at depths below six kilometers. These areas correspond to the high-slip patches located at 80 and 128 kilometers in Figure 7.5. In between, at 106 kilometers, there are negative differences with values from -1 to -2.5 meters. Above a depth of 6 kilometers, the pattern reverses: negative differences at 80 and 128 kilometers and positive differences at 106 kilometers.

The most striking difference between the two models is the shift in the depth of the high-slip patch at 128 kilometers. I found that the difference between the models resulted from a 15-kilometer by 10-kilometer area of speckle tracking data in the southeast quadrant of the image area, which shows displacements of ~ -1.5 to -2 meters in the LOS direction. Removing these points from the dataset and re-running the inversion shifted the slip upwards but only decreased the rms differences between the model predictions and the data by 1-2%. There are no GPS measurements in the area

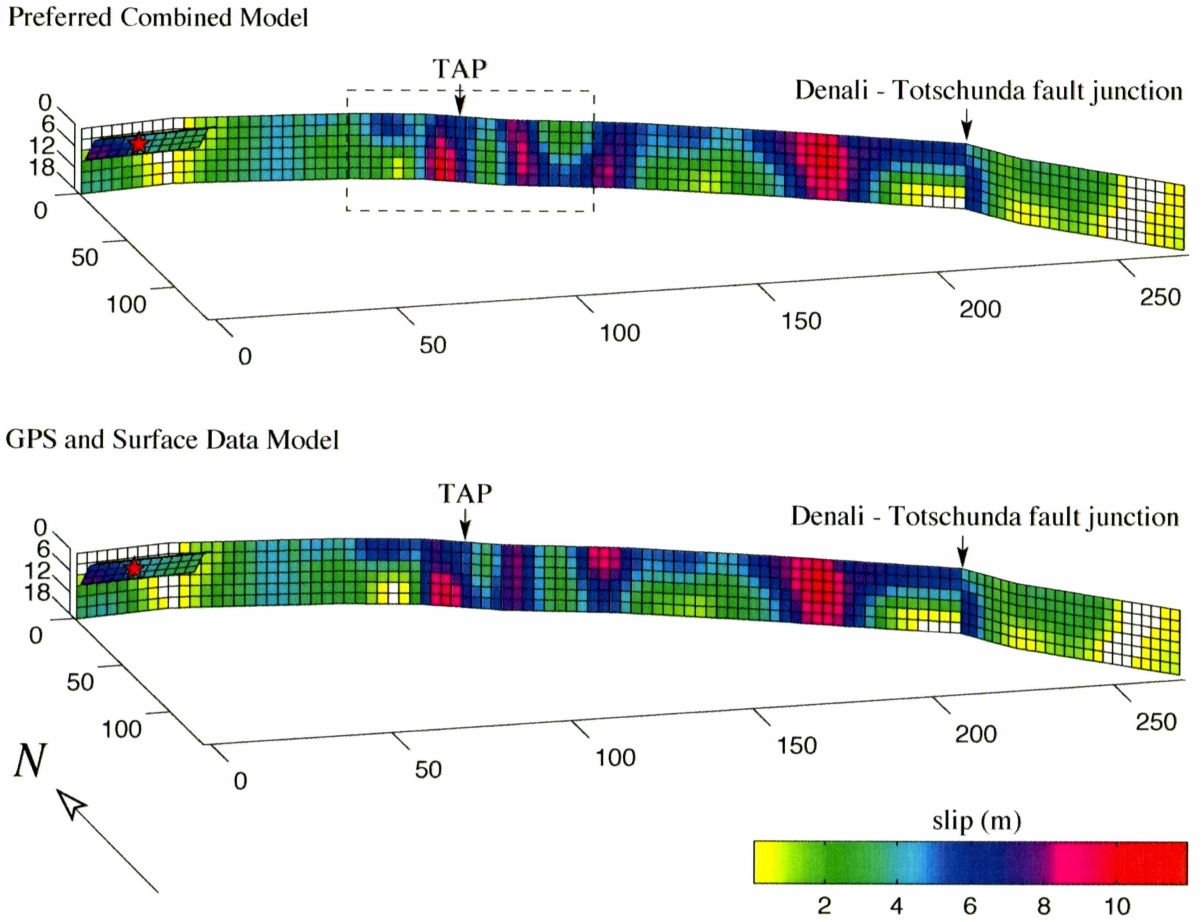

Figure 8.1. Comparison between the combined model and the GPS-derived model. The Trans-Alaska Pipeline (TAP) and the Denali-Totschunda fault junction are shown for reference. The epicenter of the earthquake is shown by the red star. Dashed box shows the extent of the speckle tracking data.

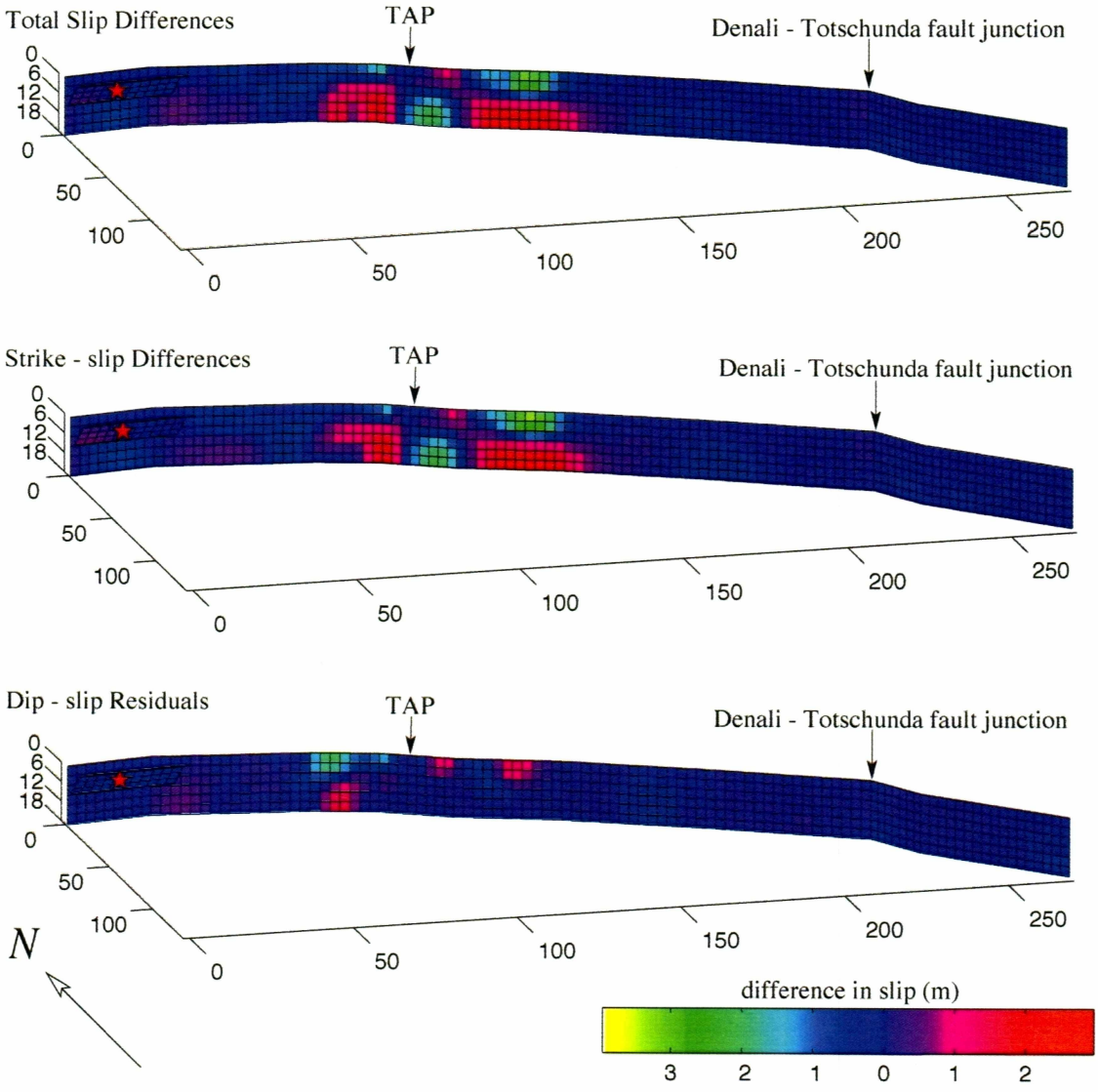

Figure 8.2. Model Differences. A positive difference indicates that the combined model predicts larger slip values than the model of *Hreinsdóttir* [2005]. The Trans-Alaska Pipeline (TAP) and the Denali-Totschunda fault junction are shown for reference. The epicenter of the earthquake is marked by the red star.

with which to directly compare the speckle tracking data points and the two models fit the available GPS data equally well. I have no reason to doubt the reliability of these points. On these grounds I decided not to remove the data points, but to regard the shift in high slip as a real result instead.

Compared to slip models using InSAR data [*Wright et al.*, 2004], regional seismic data [*Oglesby et al.*, 2004; *Dreger et al.*, 2004], and teleseismic data [*Ozacar and Beck*, 2004], the combined model shows the same general features. All of the models display a thrust event on the Susitna Glacier fault and a patch of lateral slip exceeding 8 meters on the Denali fault about 40 kilometers east of its junction with the Totschunda fault. As *Hreinsdottir* [2005] pointed out, models using geodetic or regional seismic data find an additional strike-slip sub-event near the Trans-Alaska Pipeline. The model of *Hreinsdottir* [2005] and combined model resolve three patches of high slip within this sub-event (see above and Section 7.4) while the InSAR and regional seismic models show two major slip peaks in this area. *Oglesby et al.* [2004] inverted geologic surface measurements [*Eberhart-Phillips et al.*, 2003], GPS measurements from 38 sites [*Hreinsdóttir et al.*, 2003], and local seismic waveform data to estimate the coseismic slip distribution. Their GPS-only inversion has a patch of high slip centered at about 95 kilometers from the epicenter and at a depth of 10 kilometers as well as a shallower slip patch at 145 kilometers where the highest slip occurs at the surface. In their combined GPS and seismic model, the first patch becomes shallower while the second patch, now centered at 140 kilometers, deepens, displaying over seven meters of slip at a depth of 15 kilometers. This latter patch is quite similar to the third patch of high slip in the combined model discussed earlier in this section. The kinematic slip model of *Dreger et al.* [2004] also shows an approximately 15-kilometer-deep patch of slip in this area. As the GPS data are not sensitive to details of the slip distribution at this location, the models including seismic data may provide more robust results. The seismic information supports the idea that the deep slip patch seen in the combined model is a real result rather than an error caused by a biased subset of the SAR data.

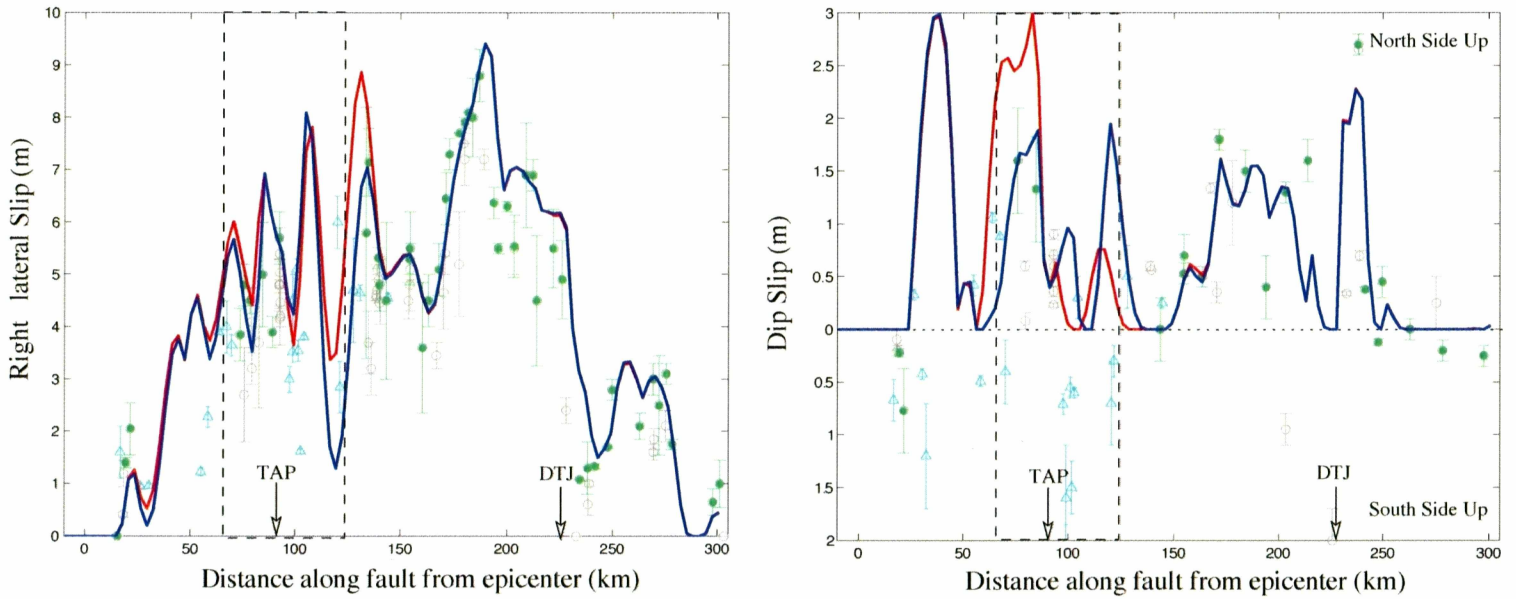

Figure 8.3. Comparison between geologic data and models. Hollow blue triangles show glacier offset measurements, hollow grey circles represent non-glacier geologic surface offsets not used in the inversion model, and solid green circles show the geologic measurements used in the models. All the geologic data are from *Haeussler et al.*, [2004]. The blue line is the estimate of the combined model while the red line is the predicted slip of the model of *Hreinsdóttir* [2005]. The Trans-Alaska Pipeline (TAP) and the Denali-Totschunda fault junction (DTJ) are shown for reference.

Figure 8.3 shows the comparison between the geologic data measurements, predictions from the model of *Hreinsdóttir* [2005], and this study's model for both lateral slip and dip slip. As expected, the two models coincide beyond the limits of the speckle tracking data. Near and within the area covered by the SAR data, however, there are several striking differences. Immediately outside the boundary of the SAR scene, there is a two-meter difference between the two models in the right-lateral strike-slip plot at about 130 kilometers from the epicenter. The GPS/geologic data model predicts a very high slip of about nine meters, a value well beyond the largest geologic surface measurement in the area. There are no GPS data near this area, so this peak is almost certainly due to smoothing used in the model. The combined model, on the other hand, estimates a peak slip of about 7 meters, a value that agrees well with the geologic surface data and fits within the maximum slip envelope calculated by *Haeussler et al.*, [2004]. Although this area is outside the SAR scene, the close proximity of speckle data to the west supplied constraints to the model here.

Within the speckle tracking coverage area, the most striking difference between the two models occurs at about 120 kilometers east of the epicenter, where the combined model estimates a slip value over two meters lower than that predicted by the GPS/geologic data model. An examination of the speckle tracking data reveals a significant decrease in displacement values in this area. I took three fault-normal profiles in the neighborhood of the minimum slip value and fitted simple screw dislocation models to each (Figure 8.4 a, b, c, and d). For ease of comparison, I then combined the three models in a single plot (Figure 8.4 e). The models clearly show a sharp decrease in the magnitude of the LOS displacements towards the location of the minimum slip value. The third profile shows an offset across the fault of 2 meters measured in the radar's LOS, which roughly translates to 2.8 meters of right-lateral surface slip. This value falls between the two model estimates shown in Figure 8.3. Lack of data prevents taking a profile at the actual location of the minimum slip value, which is slightly east of the third profile. Based on these results, I believe the drop in right-lateral slip values is real rather than an effect of the smoothing used in the model. In the dip-slip plot, the largest

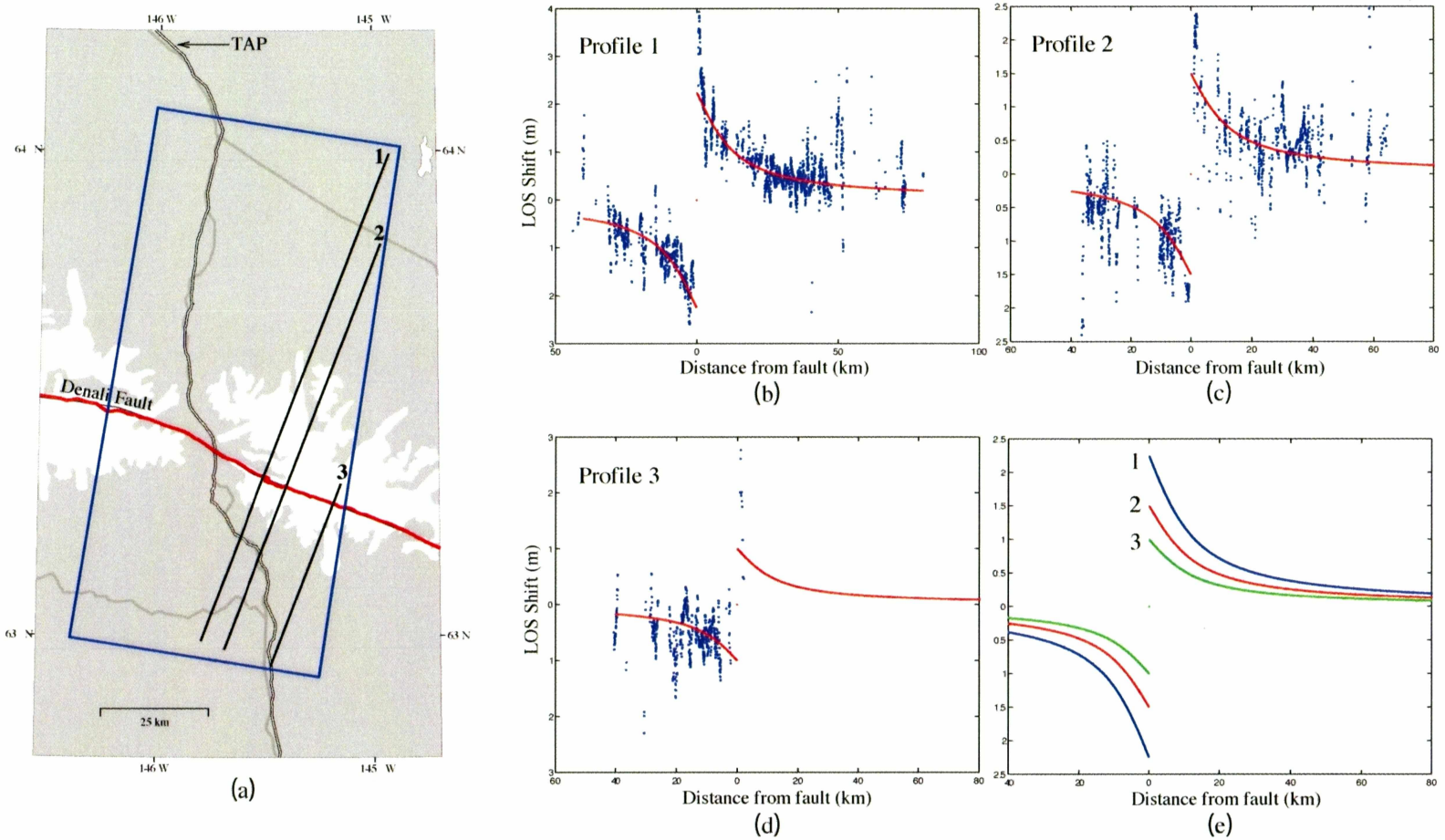

Figure 8.4. Cross-strike profiles showing decrease in offset values. (a). Map showing location of profiles. Black lines represent the profiles, the red line is the rupture, and the blue box marks the limits of the speckle tracking data. (b-d). Cross-strike profiles at each of the location. Blue dots are the speckle tracking data and the red lines are the screw dislocation models. (e). Combined plot of screw dislocation models for each profile.

difference between the two models is the peak from 50-90 kilometers along the fault from the epicenter. As in the lateral-slip plot, the GPS/geologic data model estimates high slip amounts that far exceed the geologic measurements and are likely caused by model smoothing. The combined model of the present study predicts lower slip values that fit the geologic data extremely well.

The addition of the speckle tracking data to the inversion provided important constraints to the model in the region with the highest variability of slip (between about 55 and 150 kilometers from the epicenter) and a complex fault geometry. The combined coseismic slip distribution (Figure 7.5) shows a patch of high slip at about 85 kilometers east of the epicenter. Slip values approach 10 meters at depth and reach about 7 meters at the surface. This peak occurs just east of a releasing bend in the fault located at 80 kilometers from the epicenter, a place where the average strike of the fault changes from 106° to 120°. This change in strike orients the fault so that it is at smaller angle to the maximum compressive stress, a condition that results in decreased normal stress and/or increased shear stress. Prior to the Denali Fault earthquake, the regional stress regime around this bend was more favorable to strike-slip faulting than neighboring sections of the fault where the maximum compressive stress occurred almost normal to the fault [*Ratchkovski et al.*, 2004]. It is likely that the high- slip patch observed at kilometer 80 is a result of the releasing bend and the associated orientation of the regional stress field. *Hreinsdóttir* [2005] also attributed the high-slip patch to the presence of the releasing bend. Compared to her model, my model shows up to two meters more slip below a depth of six kilometers in this area. The area around the releasing bend also shows the second highest moment pulse along the length of the rupture [*Hreinsdóttir*, 2005; *Frankel*, 2004].

East of this high slip patch, my slip distribution displays a patch of lower slip at all depths that persists to kilometer 105, where another high-slip patch occurs. The average strike of the fault changes from 120° to 110° at about kilometer 100, creating a restraining bend. This decrease in average strike orients the fault in a direction that is at a greater angle to the maximum compressive stress, causing an increase in normal stress

and/or a decrease in shear stress. Pre-earthquake stress tensors show the maximum compressive stress directed nearly perpendicular to the fault in this location, a condition that favors thrust faulting [*Ratchkovski et al.*, 2004]. As Figure 8.3 shows, the dip-slip component of the total slip has a peak at this location while the strike-slip component sharply decreases. This local stress regime most likely caused the drop in slip seen in the model. My model predicts even lower slip in this region than the model of *Hreinsdóttir* [2005].

The effect of fault bends on rupture propagation and slip magnitude is not yet fully understood. *King and Nábelek* [1985] suggested that propagation around a fault bend might cause an earthquake to terminate. Based on strike-slip fault geometry and earthquakes in Turkey, *Barka and Kadinsky-Cade* [1988] proposed that ruptures could continue to propagate after they negotiate a bend in the fault. Modeling the effect of a restraining bend on a propagating crack, *Bouchon and Streiff* [1997] found that the bend caused a reduction in the overall slip. *Harris et al.* [2002] pointed out that the 1999 Izmit earthquake, which continued around a restraining bend of nearly 30°, provided clear evidence that bends do not always stop the rupture. The fault geometry and slip distribution for the Denali Fault earthquake show that earthquakes can propagate around both releasing and restraining bends and that restraining bends can cause a drop in the slip magnitude, supporting the findings of *Barka and Kadinsky-Cade* [1988] and *Bouchon and Streiff* [1997]. In addition to this, the GPS/geologic data slip model and the slip model of this study suggest that releasing bends may influence the location of asperities. This has important implications for the evaluation of seismic hazards. As mentioned above, the high slip patch located just east of the releasing bend at kilometer 80 was associated with the second largest moment release pulse during the Denali earthquake as well as some of the largest surface offsets measured in the central section of the rupture. An examination of possible earthquake hazards on a fault should take fault geometry, particularly the location of significant releasing bends, into consideration.

9 Conclusions

In this thesis, I used SAR speckle tracking data to analyze the coseismic surface displacements of the 2002 Denali Fault earthquake and improve the GPS-derived slip model of *Hreinsdóttir* [2005].

The speckle tracking offset map vividly defines the rupture and shows a general increase in the magnitude of the displacements from west to east. A cross-strike profile near the intersection of the Denali fault with the Trans-Alaska Pipeline displays a LOS offset across the fault of 4 meters, which roughly translates to 6 meters of slip. Along-strike profiles in the western half of the speckle tracking image show spatially varying displacement magnitudes, with overall lower displacement values on the south side of the fault. In both the cross-strike and along-strike profiles, the speckle tracking data agree very well with predictions from the GPS-based model of *Hreinsdóttir* [2005] in areas with dense GPS arrays. I also converted the along-strike profile data into a speckle tracking lateral slip estimate. This estimate suggests that, taken as a whole, the glacier offset measurements underestimate the total slip and that the largest geologic offset in each local area gives the best approximation of the slip.

I inverted the speckle tracking data with the GPS data and geologic surface offset measurements used in *Hreinsdóttir* [2005] to estimate the coseismic slip distribution along the Susitna Glacier, Denali, and Totschunda faults. The highly variable slip distribution has a total moment of 6.85×10^{20} N•m (assuming a rigidity of 30 GPa) that corresponds to an M_w 7.89 earthquake. Outside the region covered by the SAR data, the combined model predictions are virtually indistinguishable from those of the GPS-derived model: about 4.5 meters of dip-slip motion on the Susitna Glacier fault, strike-slip motion of ~ 0-4 meters on the Denali fault between 0 and 60 kilometers east of the epicenter, a high-slip patch with surface slip values exceeding 9 meters located about 40 kilometers west of the Denali-Totschunda fault junction, and relatively low (less than 3.5 meters), shallow strike-slip motion on the Totschunda fault. Within and immediately surrounding the speckle tracking coverage area, however, the SAR data provide

important constraints to the model. The largest differences occur near the eastern edge of the speckle tracking image. At about 120 kilometers east of the epicenter, the combined model predicts a sharp drop in the slip that falls below the GPS model estimate. The existence of the slip decrease is supported by several cross-strike profiles of the speckle tracking data scene in that area. East of the minimum slip value, at about 130 kilometers, the combined model estimates a deeper slip patch than the GPS model, leading to lower surface slip. The high surface slip seen in the GPS model is most likely due to the smoothing constraint used in the model since there are no GPS or geologic offset data in the area. The addition of the speckle tracking data to the inversion model added valuable constraints that forced the model to conform to the data rather than simply following the smoothest path possible. The combined model's surface slip predictions show excellent agreement with the geologic surface data.

An examination of the correlations between the slip distribution and the fault geometry reveals that fault bends can impact the magnitude of the slip. In particular, releasing bends may influence the location of asperities and associated peaks in moment release.

Overall, this study has shown that speckle tracking is a valuable tool for the study of earthquakes and fault mechanics and extended the scope of previous speckle tracking studies. Those studies only used azimuth offsets since they had lower uncertainties and less noise than range offsets. This study, however, proves that range offsets can provide useful information if high resolution fine mode radar data is used. The range offset map clearly traces the rupture, and could give an estimate of the fault geometry if it wasn't already known. Speckle tracking data provide information in the crucial region closest to the fault where the InSAR data were incoherent. While having larger uncertainties than the GPS data, the speckle tracking data are robust enough to substitute for GPS measurements in regions with sparse or non-existent networks. Speckle tracking lateral slip estimates can serve as both complements and checks to the geologic surface offset data. The speckle tracking offsets can add essential constraints to a slip distribution model so that the data will have a greater influence than the smoothing constraint.

In remote regions where ground-based data doesn't exist, speckle tracking offsets alone could reliably map the rupture and be used to develop a first-order estimate of the slip distribution. In areas with more extensive data availability, a combination of GPS data, geologic surface offset data, and InSAR data, speckle tracking data can provide a complete, detailed picture of an earthquake's slip distribution at the surface and at depth.

References

Barka, A.A., and K. Kadinsky-Cade (1998), Strike-slip fault geometry in Turkey and its influence on earthquake activity, *Tectonics*, *7*, 663-684.

Bouchon, M., and D. Streiff (1997), Propagation of a shear crack on a nonplaner fault: a method of calculation, *Bull. Seis. Soc. Am.*, *87*(1), 61-66.

Crone, A.J., S.F. Personius, P.A. Craw, P.J. Haeussler, and L.A. Staft (2004), The Susitna Glacier Thrust Fault: Characteristics of Surface Ruptures on the Fault that Initiated the 2002 Denali Fault Earthquake, *Bull. Seis. Soc. Am., 94*(6B), S5-S22.

Doser, D.I. (2004), Seismicity of the Denali-Totschunda fault zone in central Alaska (1912-1988) and its relation to the 2002 Denali Fault earthquake sequence, *Bull. Seis. Soc. Am., 94*(6B), S132-S144.

Dreger, S. D., D. D. Oglesby, R. Harris, N. Ratchkovski, and R. Hansen (2004), Kinematic and dynamic rupture models of the November 3, 2002 MW7.9 Denali, Alaska, earthquake, *Geophys. Res. Lett.*, *31*(4), doi:10.1029/2003GL018333.

Eberhart-Phillips, D., et al. (2003), The 2002 Denali Fault Earthquake, Alaska: A Large Magnitude, Slip-Partitioned Event, *Science, 300*, 1113-1118.

Fletcher, H.J. (2002), Tectonics of interior Alaska from GPS measurements, Ph.D. thesis, 257 pp., Univ. Alaska Fairbanks, Fairbanks, Alaska.

Fletcher, H.J., J.T. Freymueller (2003), New constraints on the motion of the Fairweather fault, Alaska, from GPS observations, *Geophys. Res. Lett., 30*(3), 1139, doi:10.1029/2002GL016476.

Forbes, R.B., D.L. Turner, D.L. Smith, J.H. Stout, and F.R. Weber (1973), The Denali fault offset problem, *in* United States Geological Survey Alaska Program, 1973, United States Geological Survey, Circular 683, p. 46.

Haeussler, P.J., D.P. Schwartz, T.E. Dawson, H.D. Stenner, J.J. Lienkaemper, B. Sherrod, F.R. Cinti, P. Montone, P. Craw, A.J. Crone, and S.F. Personius (2004), Surface rupture and slip distribution of the Denali and Totschunda faults in the 3 November 2002 **M** 7.9 earthquake, Alaska, *Bull. Seis. Soc. Am., 94*(6B), S23-S52.

Harris, R.A., J.F. Dolan, R. Hartleb, and S.M. Day (2002), The 1999 Izmit, Turkey, earthquake: a 3D dynamic stress transfer model of intraearthquake triggering, *Bull. Seis. Soc. Am.*, *92*(1), 245-255.

Hickman, R.G., C. Craddock, and K.W. Sherwood (1977), Structural geology of the Nenana River segment of the Denali fault system, central Alaska Range, *Geol. Soc. Am. Bull., 88*, 1217-1230.

Hreinsdóttir, S., J.T. Freymueller, R. Bürgmann, and J. Mitchell, Coseismic Deformation of the 2002 Denali Fault Earthqauke: Insights from GPS Measurements, submitted to *J. Geophys. Res.*

Hreinsdóttir, S. (2005), Coseismic deformation of the 2001 El Salvador and 2002 Denali Fault Earthquakes from GPS geodetic measurements, Ph.D. thesis, 122 pp., Univ. Alaska Fairbanks, Fairbanks, Alaska.

Hreinsdóttir, S., J.T. Freymueller, H.J. Fletcher, C.F. Larsen, and R. Bürgmann (2003), Coseismic slip distribution of the 2002 M_w7.9 Denali fault earthquake, Alaska, determined from GPS measurements, *Geophys. Res. Lett., 30*(13), 1670, doi:10.1029/2003GL017447.

Jónsson, S., H. Zebker, P. Segall, and F. Amelung (2002), Fault Slip Distribution of the 1999 M_w 7.1 Hector Mine, California, Earthquake, Estimate from Satellite Radar and GPS Measurements, *Bull. Seis. Soc. Am., 92*(4), 1377-1389.

King, G., and J. Nabelek (1985), Role of fault bends in the initiation and termination of earthquake rupture, *Science, 228*, 984-987.

Lanphere, M.A. (1978), Displacement history of the Denali fault system, Alaska and Canada, *Can. J. Earth Sci., 15*, 817-822.

Matmon, A., D. Schwartz, H. Stenner, J. Lienkamper, T. Dawson, P. Haeussler, L. Staft, and R. Finkel, Determining Holocene and late Pleistocene slip rates along the Denali fault using cosmogenic ^{10}Be analysis of boulders on displaced moraines, *Geol. Soc. Am. Abstracts with Programs*, *36*(5), 137.

Matthews, M., and P. Segall (1993), Statistical inversion of crustal deformation data and estimation of the depth distribution of slip in the 1906 earthquake, *J. Geophys. Res.*, *98*(B7), 12,153-12,163.

Michel, R., J.-P. Avouac, and J. Taboury (1999a), Measuring ground displacements from SAR amplitude images: application to the Landers earthquake, *Geophys. Res. Lett.*, *26*(7), 875-878.

Michel, R., J.-P. Avouac, and J. Taboury (1999b), Measuring near field coseismic displacements from SAR images: application to the Landers earthquake, *Geophys. Res. Lett., 29*(19), 3017-3020.

Moick, J.G. (1980), Digital processing of remotely-sensed images, *NASA SP-431*, 187-197.

Nokleberg, W.J., D.L. Jones, and N.J. Silberling (1985), Origin and tectonic evolution of the Maclaren and Wrangellia terranes, eastern Alaska Range, Alaska, *Geol. Soc. Am. Bull., 96*, 1251-1270.

Oglesby, D. D., D. S. Dreger, R. A. Harris, N. Ratchkovski, and Roger Hansen (2004), Inverse kinematic and forward dynamic models of the 2002 Denali, Alaska earthquake, *Bull. Seis. Soc. Amer.*, *94*(6B), S214-S233.

Okada, Y. (1985), Surface deformation due to shear and tensile faults in a half-space, *Bull. Seis. Soc. Am.*, *75*(4), 1135-1154.

Ozacar, A.A. and S. Beck (1994), The 2002 Denali Fault and 2001 Kunlun Fault earthquakes: Complex rupture processes of two large strike-slip events, *Bull. Seis. Soc. Am., 94*(6B), S278-S292.

Page, R.A. (1972), Crustal deformation on the Denali Fault, Alaska, 1942-1970, *J. Geophys. Res., 77*(8), 1528-1533.

Peltzer, G., F. Crampé, and G. King (1999), Evidence of Nonlinear Elasticity of the crust from the M_w7.6 Manyi (Tibet) Earthquake, *Science, 286*, 272-276.

Plafker, G., and H.C. Berg (1994), Overview of the geology and tectonic evolution of Alaska, *in* Plafker, G., and H.C. Berg, eds., The Geology of Alaska: Boulder, Colorado, Geological Society of Amercia, The Geology of North America, G-1.

Plafker, G., L. Gilpin, and J. Lahr (1994), Neotectonic map of Alaska, Map in The Geology of North America, Decade of North American Geology, vol. G-1, edited by G. Plafker and H. C. Berg, Geol. Soc. Amer., Boulder, Colorado.

Plafker, G., G. Carver, M. Metz, and L. Cluff (2004), Repeated historic surface ruptures of the Denali fault at Delta River, Alaska during large earthquakes in 1912 and 2002, *Eos Trans. AGU, 85*(47), Fall Meet. Suppl., Abstract G11A-0780.

Price, E.J., and R. Bürgmann (2002), Interactions between the Landers and Hector Mine, California, earthquakes from space geodesy, boundary element modeling, and time-dependent friction, *Bull. Seis. Soc. Am.*, *92*(4), 1450-1469.

Ratchkovski, N.A., S. Wiemer, and R.A. Hansen (2004), Seismotectonics of the central Denali fault, Alaska, and the 2002 Denali Fault earthquake sequence, *Bull. Seis. Soc. Am.*, *94*(6B), S156-S174.

Reed, B.L., and M.A. Lanphere (1974), Offset plutons and history of movement along the McKinley segment of the Denali fault system, Alaska, *Geol. Soc. Am. Bull., 85,* 1883-1892.

Richter, D.H., and N.A. Matson (1971), Quaternary faulting in the eastern Alaska Range, *Geol. Soc. Am. Bull., 82,* 1529-1540.

Savage, J.C., and M. Lisowski (1991), Strain accumulation along the Denali Fault at the Nenana River and Delta River crossings, Alaska, *J. Geophys. Res.*, *96*(B9), 14,481-14,492.

Savage, J.C. (1990), Equivalent strike-slip cycles in half-space and lithosphere-asthenosphere earth models, *J. Geophys. Res.*, *95*, 4873-4879.

Stark, P. B., and R. L. Parker (1995), Bounded-variable least-squares: An algorithm and application, *Comput. Stat.*, *10*(2), 129-141.

Stout, J.H., J.B. Brady, F. Weber, and R.A. Page (1973), Evidence for Quaternary movement on the McKinley strand of the Denali Fault in the Delta River area, Alaska, *Geol. Soc. Am. Bull., 84*, 939-948.

Turner, D.L, T.E. Smith, and R.B. Forbes (1974), Geochronology of offset along the Denali fault system in Alaska, *Geol. Soc. Am. Abstracts with Programs, 6,* 268-269.

Wessel, P., and W. H. F. Smith (1998), New improved version of the Generic Mapping Tools relseased, *Eos. Trans. AGU*, *79*(47), 574.

Wright, T.J., Z. Lu, and C. Wicks (2004), Constraining the slip distribution and fault geometry of the M_w 7.9, 3 November 2002, Denali Fault Earthquake with InSAR and GPS, *Bull. Seis. Soc. Am., 94*(6B), S175-S189.